



Wind-cloud interactions observed with Aeolus spaceborne Doppler Wind Lidar

Zacharie Titus¹, Marine Bonazzola¹, Hélène Chepfer¹, Artem G. Feofilov¹, Marie-Laure Roussel¹, Benjamin Witschas², Sophie Bastin³

- ¹Laboratoire de Météorologie Dynamique/Institut Pierre Simon Laplace (IPSL), Sorbonne Université, CNRS, Institut Polytechnique de Paris, Paris, France
 - ²Deutsches Zentrum für Luft- und Raumfahrt e.V. (DLR), Institut für Physik der Atmosphäre, 82234 Oberpfaffenhofen, Germany
 - ³Laboratoire ATmosphere Milieux Observations Spatiales/Institut Pierre Simon Laplace (IPSL), UVSQ Université Paris-Saclay, Sorbonne Université, CNRS, CNES, Guyancourt, France

Correspondence to: Zacharie Titus (<u>zacharie.titus@lmd.ipsl.fr</u>)

Abstract. Model based studies have shown interactions between wind vertical profiles and cloudiness, but few observational studies corroborate them. The unique observations of Aeolus spaceborne Doppler wind lidar can contribute to fill this gap. In this paper, we merged global Aeolus observations of cloud profiles at full horizontal resolution (3 km along orbit track) with co-located profiles of horizontal winds.

We first observed wind-cloud interactions at regional scale over the Indian Ocean. Aeolus captures the strengthening of the Tropical Easterly Jet in early June 2020, with wind speeds exceeding 40 ms⁻¹ in its core, and a simultaneous increase of high cloud fraction up to above 30 %, until the decay of the jet during fall.

Secondly, we observed wind-cloud interactions at cloud scale (between 3-100 km) in different regions. Over the Indian Ocean as well as over cumulus and stratocumulus dominated regions, we found that the wind shear in cloudy sky is always smaller than the wind shear in the clear sky surrounding the cloud (statistically significant). In addition, we found that the wind speed difference between the cloud and its surrounding clear sky increases with the clear sky wind shear, especially in cumulus (R=0.93) and stratocumulus (R=0.89) dominated regions. This study demonstrated that despite its coarse resolution, Aeolus can capture wind perturbations induced by convective momentum transport.





1 Introduction

Clouds play a critical role in Earth's climate as a major component of the water vapor cycle and because they have a large impact on the radiative budget at the top of the atmosphere and at the Earth surface. The formation and development of clouds are controlled by the surface temperature and by the thermodynamic structure of the lower troposphere, but also by dynamic variables. It was shown that fast horizontal winds are responsible for an increased cirrus cloud cover through different mechanisms like advection of humidity from warmer to cooler regions, favoring the in-situ formation of cirrus clouds (Das et al., 2011). Deep convective cloud systems tend to form in regions of large-scale wind convergence. They organize into rain bands and squall lines by the wind shear (e.g., Thorpe et al., 1982; Rotunno et al., 1988; Parker, 1996; Hildebrand, 1998; Robe and Emanuel, 2001; Weisman and Rotunno, 2004; Abramian et al., 2022). The wind shear can also inhibit deep and shallow convection by "blowing off" cloud tops (e.g., Koren et al., 2010; Sathiyamoorthy et al., 2004), or increase the cloud cover by tilting cloud tops away from their base (Mieslinger et al., 2019), thus influencing cloud-top height and cloud cover (Helfer et al. 2020). Over marine boundary layers, the wind shear can even locally deplete stratocumulus cloud tops (Wang et al. 2008; Schulz and Mellado, 2018). Reversely, clouds can have an influence on winds through their radiative effect. Fujiwara et al. 2004 showed that the radiative cooling associated to anvils creates a temperature gradient at the top of high convective clouds, that can generate a thermal wind. At a large scale, it was shown that the cloud radiative effect impacts the intensity and location of the jet stream by altering temperature gradients and redistributing energy within the atmosphere (Voigt et al, 2021).

To better understand wind-cloud interactions, a large number of studies have been performed. These studies are based on models or meteorological analyses. Observations of winds within cloudy systems are usually performed by radiosondes, airborne or ground based Doppler Radars, and are therefore limited in space and time. In this study, we benefit from the unique capabilities of the Atmospheric LAser Doppler INstrument (ALADIN), a 355 nm spaceborne Doppler Wind Lidar with High Spectral Resolution (HSRL) capabilities onboard the Aeolus satellite (Stoffelen et al., 2005; Reitebuch et al., 2012). Aeolus is primarily designed to retrieve profiles of horizontal winds but can also retrieve profiles of clouds (Flamant et al., 2008; Dabas et al., 2022; Feofilov et al., 2022). During its 5 years of operation (Aeolus DISC, 2024), Aeolus scanned over a billion kilometers of atmosphere around the globe, encountering all kinds of cloudy systems at various latitudes. Aeolus thus offers for the first time the possibility to analyze, at global-scale, co-located instantaneous profiles of clouds and profiles of horizontal winds within clouds and their clear sky surroundings.

In its current state, studying wind-cloud interactions with Aeolus is challenging for two reasons. First of all, clouds can be as little as a few tens of meters horizontally (Koren et al., 2008), cloud detection thus needs to be performed at the highest



70

80

85



possible spatial resolution in order to avoid mixing clear and cloudy scenes. Recent work showed that it is possible to perform cloud detection at full horizontal resolution of 3 km (Donovan et al., 2024b; Wang et al., 2024). We thus developed a cloud detection similar to theirs at 3 km of resolution along the orbit track using Aeolus Level 1A (L1A) data which contains the uncalibrated backscatter signal. Compared to the approach introduced by Donovan et al., 2024b, we apply slight differences such as a compensation of the missing cross-polar signal of Aeolus from a climatology of the GCM-Oriented Cloud-Aerosol Lidar and Infrared Pathfinder Satellite Observation Cloud Product (CALIPSO-GOCCP) observations, as well as the systematic discarding of hot pixels. Secondly, the wind profiles are available in a different Aeolus product with a different along-track resolution, therefore an additional processing is necessary to merge clouds and winds.

Aeolus is primarily designed to retrieve vertical profiles of horizontal winds in the troposphere and the lower stratosphere at global-scale. The laser is pointed 35° off-nadir and perpendicular to the satellite track, away from the Sun. The obtained measurement is not the actual horizontal wind $\overline{U(z)} = \overline{u(z)} + \overline{v(z)}$, but its projection on the laser pointing direction $U_{proi}(z) = |\overrightarrow{U(z)}|_{cos}(\varphi)$ where u and v are the zonal and meridional winds wind and φ the angle between the actual horizontal wind direction and the laser pointing direction (Fig. 1), also called the line-of-sight (LOS) in Aeolus literature. Hereafter, we use the wind profiles from Aeolus Level 2B (L2B, Baseline 16) scientific wind product which have been continuously validated during the mission with airborne lidars (Lux et al., 2020; Witschas et al., 2020; Witschas et al., 2022), ground based lidars, radars and radiosondes (Ratynski et al., 2023; Iwai et al., 2021; Belova et al., 2021; Baars et al., 2020). Aeolus wind profiles come from two channels, A "Mie channel" retrieves wind within entire optically thin clouds, which cover typically 35 % of the globe on average (Guzman et al., 2017) but also within the upper layers of opaque clouds, which cover typically 31 % of the globe on average. The "Rayleigh channel" retrieves wind in clear sky, which covers the remaining 34 % of the globe on average. The Rayleigh and Mie channels have horizontal and vertical resolutions that vary to optimize the signal to noise ratio and vertical coverage. The latest validation campaigns of Aeolus showed that the systematic error (bias) for wind measurements remained within the mission requirements of 0.7 ms⁻¹ for both Mie and Rayleigh channels, while the random error was about 3 ms⁻¹ for the Mie channel and 5 to 7 ms⁻¹ for the Rayleigh channel. In order to fully benefit from Aeolus observations to better understand wind cloud interactions, it is necessary to use statistical approaches with a large number of independent wind profiles in order to reduce the impact of the random error (reduced by a factor N^{1/2} with N independent profiles).

The purpose of this paper is to evaluate the feasibility of studying wind-cloud interactions from large scale to cloud scale (between 3-100 km), making use of our dataset of merged global Aeolus observations of cloud profiles at full horizontal resolution (3 km along orbit track) with co-located profiles of horizontal winds. At a large scale, we particularly focus on the



115



relationship between high cloud cover and the Tropical Easterly Jet (TEJ) over India. At a lower scale, we evaluate the benefit of our observations for the study of Convective Momentum Transport (CMT).

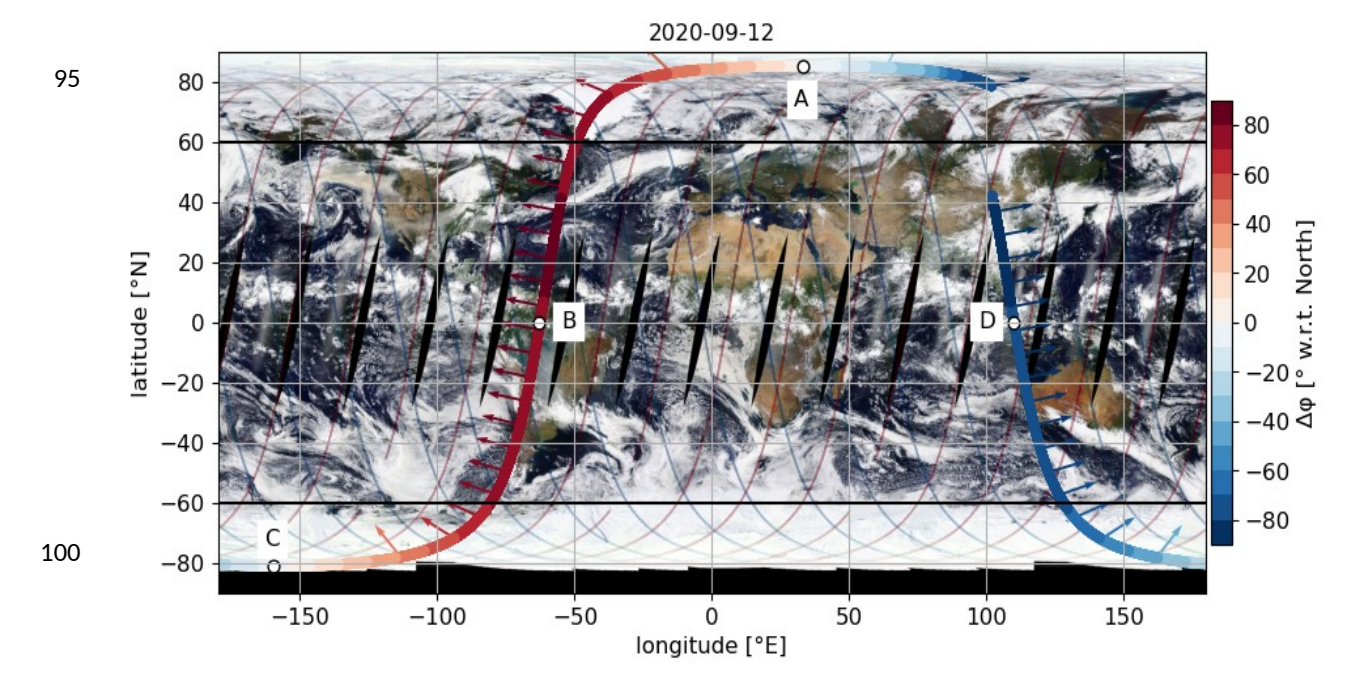


Figure 1: Track of one Aeolus orbit (2020-09-12T09 – 2020-09-12T11). Aeolus retrieves the projection of wind aligned with the vectors. Δφ represents the angle between the South-North axis and the vectors, counter-clockwise. Thinner curves represent all obits for the day of 2020-09-12. A is the North-most point. B is the equatorial crossing point during descending phase (0600 LT). C is the South-most point. D is the equatorial crossing point during ascending phase (1800 LT)

Section 2 of the paper details the method used to retrieve profiles of clouds. In Sect. 2.2 we assess the quality of this cloud detection by comparing it to another cloud climatology obtained with CALIPSO-GOCCP. In Sect. 3, we re-sample Aeolus L2B Mie and Rayleigh wind observations at 3 km of resolution along track and 480m vertically and merge them using the cloud mask. We also quantify how much of the natural "sub-grid" variability is missed when re-sampling the wind from 87 km to a sub-grid resolution of 8 km using high spatial resolution airborne Doppler Wind Lidar (DWL), and also to a sub-grid resolution of 3 km using a high spatial resolution performed with the Weather Research and Forecasting (WRF) model. Finally, in Sect. 4, we present the first descriptive results that we obtain with this dataset, focusing on different horizontal scales. We study the Tropical Easterly Jet and its correlation with high cloud fractions. We also assess the difference between cloudy and clear sky winds at cloud scales inferior to 100 km. We conclude this paper in Sect. 5.

https://doi.org/10.5194/egusphere-2025-2065 Preprint. Discussion started: 26 May 2025

© Author(s) 2025. CC BY 4.0 License.





2 Processing Aeolus clouds

2.1 Building cloud diagnostics from Aeolus from particulate and molecular backscatter profiles

We use the highest resolution Aeolus dataset (L1A), which corresponds to an on-board averaging of 16 subsequent accumulated backscatter profiles resulting in a horizontal resolution of 3 km along orbit track. To estimate the cloud mask, we process Aeolus L1A raw data at the detector level.

Even though the molecular and particulate channels of ALADIN were designed to detect the radiance backscattered from molecules and particles, respectively, this separation is not perfect. We only use the radiance retrieved by the detector of the Mie channel. Following an approach similar to that of Donovan et al., (2024b), we use the spectral leak of molecular backscatter and particulate backscatter. The spectrum of the radiance reaching the 16 pixels of the detector of the Mie channel consists of a superposition of a narrow peak related to a particulate backscatter and a several times broader peak associated with molecular backscatter (Fig. A1). The position of the center of the joint envelope represents the direction and the strength of the wind, whereas the integral of the signal is proportional to a total attenuated backscatter, and the ratio between the core and the wings of the envelope is related to particulate-vs-molecular backscatter ratio.

For a given profile, we process the spectrum measured by the detector of the Mie channel at each altitude level in six successive steps.

a) Discard "hot pixels".

135

140

It has been known since the early days of the Aeolus mission that certain pixels of the detector are damaged by cosmic particles and that the number of these pixels almost linearly increases over the mission's lifetime (Weiler et al., 2021). Even though Weiler et al., (2021) proposed a compensation method for the signals affected by hot pixels, we preferred to discard all the pixels according a hot pixel map corresponding to the end of Aeolus mission. Once the hot pixel is discarded, its value is replaced by an interpolated value of the two surrounding pixels. By doing so, we avoid potential false trends caused by a decreasing number of "normal" undamaged pixels with time.

b) Intensities of the particulate backscatter and molecular backscatter in arbitrary unit.

For each profile and each altitude level, we subtracted the average of the Detection Chain Offset (DCO, more details are given in Fig. A1) stored in the first two and last two pixels. Then, based on the peak position, we selected eight pixels either to its left or right. The signal retrieved in the pixels corresponding to the peak and the two following pixels are summed and correspond to the particulate backscatter, called $I_{part}(z_{L1A})$ here after, z_{L1A} being the altitude of the center of a layer in a L1A





profile. The signals retrieved in the six remaining pixels are summed and correspond to the molecular backscatter, called $I_{mol}(z_{L1A})$. Although the molecular or Rayleigh signal in this approach does not represent the actual molecular backscatter, it is proportional to it, enabling us to use the difference between $I_{part}(z_{L1A})$ and $I_{mol}(z_{L1A})$ to determine the cloud mask.

c) Constant vertical and horizontal resolutions.

To detect clouds consistently at all locations and all times, we need the intensities of the molecular and particulate signals at a fixed vertical and a fixed horizontal resolutions. Indeed, variations in the resolutions influence these quantities because a different volume of the atmosphere is probed. Aeolus L1A profiles have a fixed horizontal resolution (3 km) but a variable vertical resolution along the orbit. As the number of layers along the vertical is fixed (24 bins) but the altitudes of the top of the vertical profiles vary between 15 and 25 km, the vertical resolution Δz_{LIA} of Aeolus L1A layers ranges between 250 m near the surface up to 2 km in the stratosphere. We thus need to define proxies of the backscattered signals at a fixed vertical resolution $\Delta z = 480$ m, similar to the one used in CALIPSO-GOCCP (Chepfer et al. 2010), from the sea-level up to 19.2 km of altitude. These new proxies are noted $I_{part-alt}(z)$ and $I_{mol-alt}(z)$ and are defined as:

$$I_{part-alt}(z) = I_{part}(z_{L1A}) \frac{480}{\Delta z_{L1A}}$$
 (1)

$$I_{mol-alt}(z) = I_{mol}(z_{L1A}) \frac{480}{\Delta z_{L1A}}$$
 (2)

where *z* is the altitude of the center of a 480 m layer in the new vertical scale.

d) Depolarization correction.

170

ALADIN's emission is circularly polarized but the receiver is only able to measure the co-polarized component of the backscattered light. It misses the cross-polarized component. Backscattering by non-spherical particles modifies the state of polarization of light. Therefore the intensity of the particulate backscatter measured by ALADIN is underestimated within mixed phase clouds and ice clouds that contain non-spherical particles. To compensate for this, we use a monthly climatology of the depolarization ratio (δP) from CALIOP/CALIPSO observations (Feofilov et al., 2024) to correct $I_{part-alt}(z)$ as follows:

$$I_{part-alt-\delta P}(z) = \frac{I_{part-alt}(z)}{(1-\delta P)},$$
(3)

https://doi.org/10.5194/egusphere-2025-2065 Preprint. Discussion started: 26 May 2025







The output files at this stage are thus orbit files containing profiles of proxies of particulate $I_{part-alt-\delta P}(z)$ and molecular backscatter $I_{mol-alt}(z)$ at a fixed resolution of 3 km along orbit track and resampled at 480 m vertically from the surface up to 19.2 km of altitude.

e) Fully attenuated bins

For each profile, all the layers located below the lowest cloudy layer with a total backscatter $I_{part-alt-\delta P}(z) + I_{mol-alt}(z) = 0$ are flagged as fully attenuated.

f) Cloud detection.

For each profile, a layer is declared cloudy when $I_{part-alt-\delta P}(z) - I_{mol-alt}(z)$ exceeds a certain threshold. More details about the calculations of the threshold are given in appendix A and Fig. A2.

At this stage, the output files are orbit files containing a cloud mask at a 3 km along-track resolution and a 480 m vertical resolution. An example is given later in this paper (Fig. 8b)

g) From cloud mask orbits, we compute daily gridded profiles of cloud fraction over 2° latitude x 2° longitude grid boxes. For each 480 m thick layer, the cloud fraction is the ratio between the number of "cloudy" bins encountered within the grid box for the considered day at this vertical level, and the total number of non-attenuated bins observed within the same grid box at the same vertical level.

195

200





2.2 Evaluation of Aeolus clouds against a CALIPSO-GOCCP climatology

2.2.1 CALIPSO-GOCCP dataset

To assess the quality of our cloud detection, we compare it to independent cloud observations retrieved from another space lidar. The GCM Oriented CALIPSO Cloud Product from the Cloud-Aerosol Lidar and Infrared Pathfinder Satellite Observation, (CALIPSO-GOCCP, Chepfer et al., 2010) displays cloud profiles at a 333 m horizontal resolution and a 480 m vertical resolution from 2006 to 2023, and thus, overlaps the Aeolus mission during over 4 years between 2018 and 2023. We used CALIPSO-GOCCP version 3.1.4, in which low laser energy shots are discarded. An in-depth comparison between CALIPSO-GOCCP and Aeolus clouds has already been done (Feofilov et al., 2024) but using scattering ratios derived from Aeolus Level 2A calibrated optical properties data (instead of L1A data here) at a coarser resolution of 87 km along orbit track. Even though CALIOP is also a space lidar, differences between CALIOP and ALADIN listed hereafter lead to differences in cloud detection that need to be kept in mind in the comparison:

- CALIOP (Winker et al., 2004) operates at 1064 and 532 nm while ALADIN operates at 355 nm.
- CALIOP points at 3° off-nadir while ALADIN points at 35° off-nadir.
- CALIPSO follows a sun-synchronous orbit, with its ascending (resp. descending) equatorial crossing occurring at 1330 LT (resp. 0130 LT), while Aeolus ascending and descending equatorial crossings respectively occur at 1800 LT and 0600 LT. Therefore, close co-locations between the two instruments are rare, and the diurnal cycle of clouds (Noel et al., 2018; Chepfer et al., 2019), is corrected using the Cloud–Aerosol Transport System (CATS) onboard the International Space Station (McGill et al., 2015) data applied to CALIPSO-GOCCP between 60°S and 60°N as detailed in Feofilov et al., 2024.
 - The horizontal along orbit track resolution is 333m for CALIPSO-GOCCP and 3 km for Aeolus.
- CALIOP is polarization-sensitive, ALADIN is not although we compensate the particulate backscatter by a climatology of the depolarization ratio observed by CALIOP.
 - In GOCCP, the bin encompassing the surface can contain information about its cloudiness while it is systematically discarded in ALADIN.



240

245



2.2.2 Comparison of Aeolus and CALIPSO cloud climatology

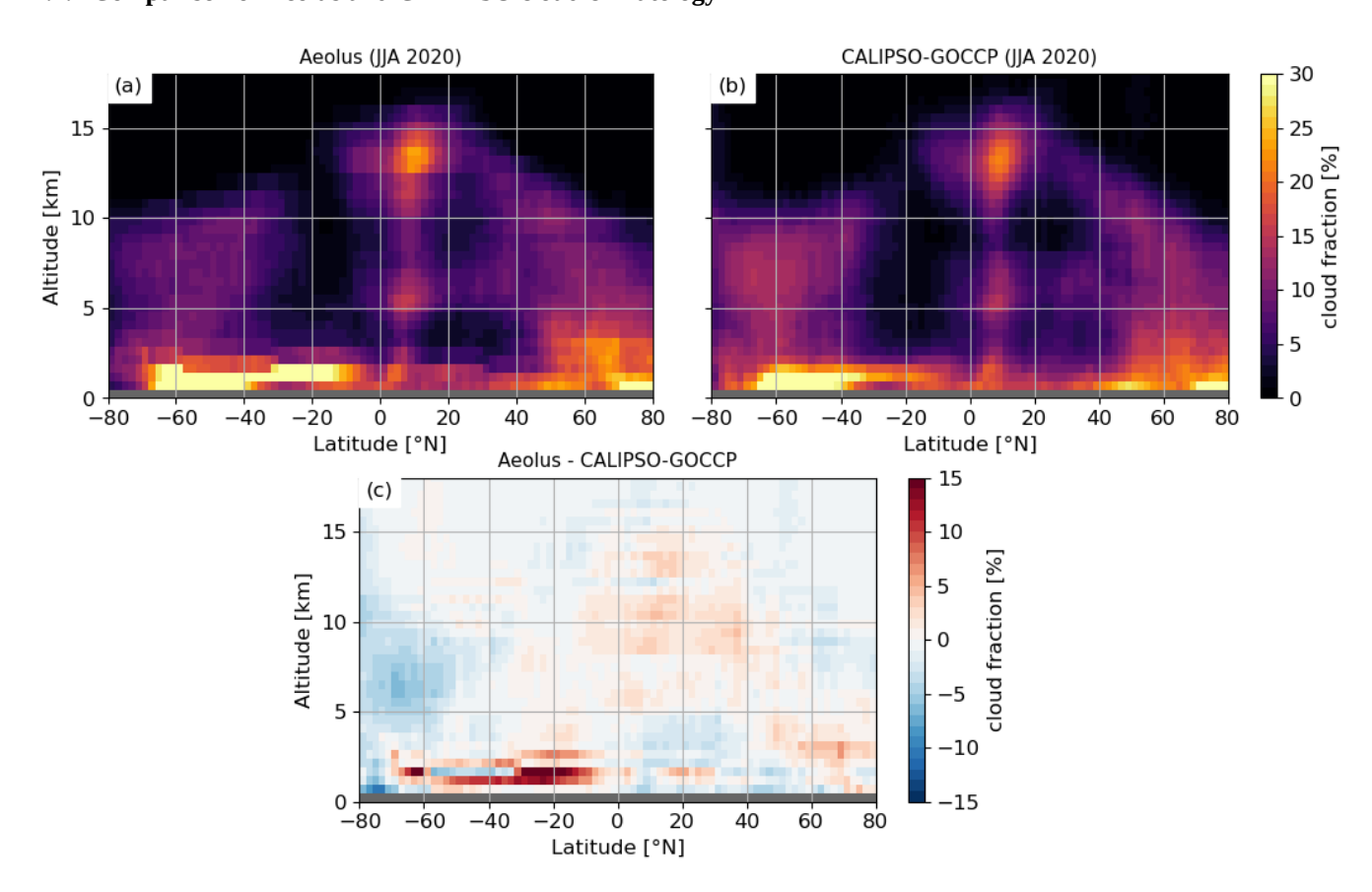


Figure 2: Zonal average of cloud fraction profiles for (a) Aeolus and (b) CALIPSO-GOCCP (c) is the absolute difference between Aeolus and CALIPSO-GOCCP. The lowest bin encompasses the surface or is under the ground and is discarded in this study (opaque gray bar).

We compare the zonal average of cloud fraction profiles retrieved from ALADIN (Fig. 2a) to those retrieved from CALIPSO-GOCCP (Fig. 2b) during boreal summer 2020. Overall, CALIPSO-GOCCP and Aeolus show similar cloud patterns. The cloud fractions are in good agreement with R²=0.79 and Pearson correlation of 0.86. In both cases a local maximum of cloud fraction of about 25 % are found around 10° N within the inter tropical convergence zone (ITCZ), between 12 and 15 km. A second maximum of 35 % is found over the Southern Ocean around 50°S in the lower troposphere (below 2.5 km). Minima of cloud fractions with Aeolus and CALIPSO-GOCCP appear within the tropical region on each side of the Equator in the middle troposphere, within the descending branch of Hadley circulation. In Fig. 2c, we see cloud fraction differences remain lower than 3 % within most of the troposphere between 60°S and 60°N. Between 1 and 2 km of altitude, Aeolus retrieves a zonal mean cloud fraction about 15 % greater than CALIPSO-GOCCP between 30°S and 10°S.





These latitudes are dominated by sparse cumulus clouds with horizontal extents smaller than 3 km. In the presence of such small clouds, CALIPSO-GOCCP sees a succession of profiles with sometimes a cloudy layer and sometimes only clear sky layers, while Aeolus only sees a 3 km profile with a cloudy layer. The effect of a coarsened horizontal resolution on cloud detection is more detailed in Chepfer et al., 2013 with cloud fractions 20 to 25 % larger for trade wind cumulus when coarsening the resolution (averaging the signal prior to cloud detection) from 330 m to 10 km, which is in the range of what we find in Fig. 2a.

3 Processing Aeolus winds

260

265

Having a dataset with Aeolus wind profiles resampled at the same fixed resolution as Aeolus cloud profiles is crucial to ease the use of these data for wind-cloud interactions studies. So far, Aeolus wind data (L2B) provided to the community are orbit files that contain 2 types of wind profiles (the Mie wind and the Rayleigh wind) estimated from the molecular and particulate backscattered signals respectively, with a varying vertical resolution (250 m to 2 km) but also a varying horizontal resolution (ranging from 3 km to 15 km in the Mie channel and fixed at 87 km in the Rayleigh channel). In this section we explain how we merge these two wind datasets making use of the cloud mask defined in Sect. 2. In a nutshell, our method consists in resampling Rayleigh and Mie winds by duplicating them at the same resolution as the cloud mask (3 km horizontally along orbit track and 480 m vertically), and then selecting the right wind (Rayleigh or Mie) based on the result of the cloud mask (clear or cloudy).

3.1 Re-sampling clear and cloudy sky winds and unifying them on a spatially regular curtain based on our cloud detection

We process the L2B Mie and Rayleigh wind profiles in four successive steps.

a) We first apply the prescribed quality controls for Aeolus L2B winds. We make sure that we only select the valid Mie winds (*validity_flag* == 1, *observation_type* == 1, *hlos_error_estimate* < 5 ms⁻¹) and the valid Rayleigh winds (*validity_flag* == 1, *observation_type* == 2, *hlos_error_estimate* < 9 ms⁻¹).



290



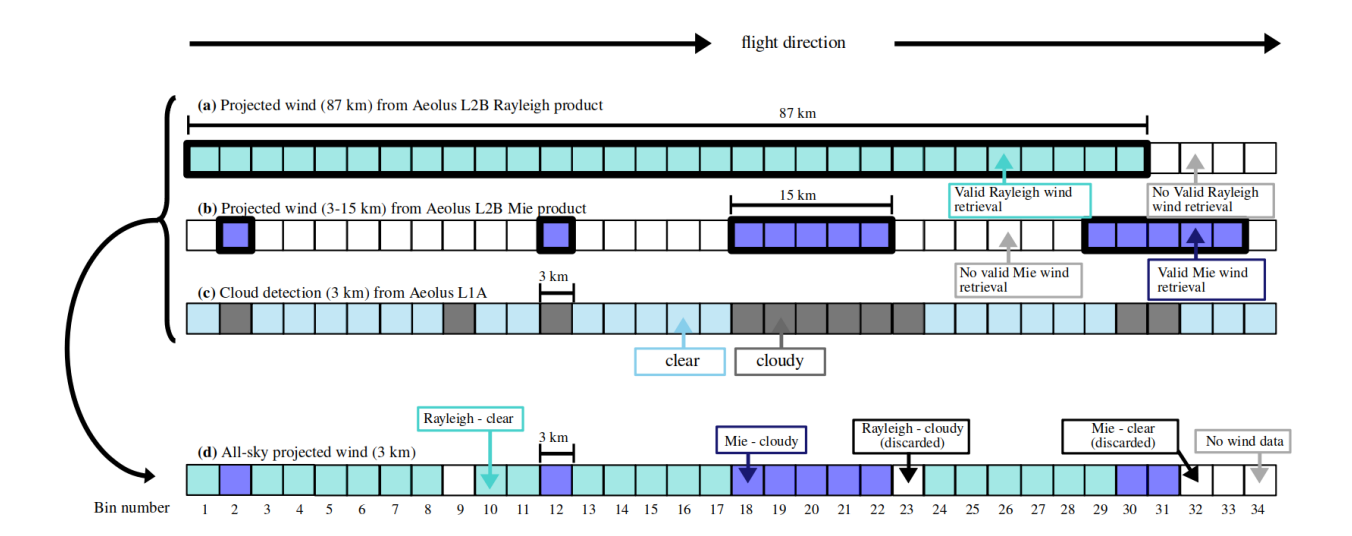


Figure 3: Building the all-sky wind along an orbit segment at one altitude level by selecting the adequate wind from Aeolus L2B based on the cloud detection. Each square represents a bin of 3 km x 480 m. (a) Blue bins contain valid wind from Aeolus L2B Rayleigh channel (87km resolution along orbit track). (b) Purple bins contain valid wind from Aeolus L2B Mie channel (3 to 15 km resolution along orbit track). (c) Cloud detection made from Aeolus L1A (3 km resolution along orbit track). (d) Aeolus all-sky wind at 3 km along orbit track resolution, built by compositing lines (a) to (c). Blue bins contain a valid clear sky wind, purple bins contain a valid cloudy sky wind and white bins contain no wind data.

b) We then display each wind at a fixed resolution of 3 km x 480 m. For each 3 km x 480 m bin, we look for the closest L2B wind from the Rayleigh channel in a limit of 87 km, which corresponds to the horizontal resolution of Rayleigh wind, and we duplicate its value (Fig. 3a). Similarly, we look for the closest L2B wind from the Mie channel in a limit of 15 km, which corresponds to the maximum horizontal resolution for the Mie wind, and we duplicate its value (Fig. 3b). We thus obtain at this stage winds from both channels re-sampled at 3 km along track and 480 m vertically. A bin can contain either a Rayleigh wind (bin 26, Fig. 3a) or a Mie wind (bin 32, Fig. 3b) or both winds (bin 2, Fig. 3a and 3b) or no wind (bin 34, Fig. 3a and 3b) in the fully attenuated bins.

c) Making use of the cloud mask (Fig. 3c), we select for each bin, either a Rayleigh (Fig. 3a) or a Mie (Fig. 3b) wind to build the all-sky wind. Consider bin 2, (Fig. 3) where both Rayleigh and Mie winds coexist. As a cloud was detected (bin 2, Fig. 3c), we select the Mie wind as an element of the all-sky wind (bin 2, Fig. 3d). For bin 29, both Rayleigh and Mie winds also coexist, however, no cloud is detected locally so we select the Rayleigh wind as the all-sky wind (bin 29, Fig. 3d). For bin 23 where a cloud is detected, with a Rayleigh wind but no Mie wind, we decide to report "no data" in the all-sky wind dataset instead of a Rayleigh wind (bin 23, Fig. 3d). In a similar way, for bin 32 which shows no Rayleigh wind but a Mie wind in



310

315

320



clear sky conditions, we report "no data" instead of a Mie wind (bin 32, Fig. 3d). By doing so, we ensure that the Rayleigh winds indeed correspond to clear sky situations and the Mie winds to cloudy sky situations, consistently with our cloud mask. From now on, we will simply call these winds "clear sky wind" and "cloudy sky wind", the all-sky wind being thus a merging of both of them.

d) Under a cloudy layer, the Rayleigh signal is so weak that the clear sky wind retrieval can not be trusted. For each profile, we therefore discard all clear sky winds located at altitudes below a cloudy layer.

At this stage, the output files are individual orbit files with a cloud mask and Aeolus cloudy, clear and all-sky winds at 3 km along-track resolution and 480 m vertical resolution.

3.2 About the sub-grid variability of wind at 3 km

At a given altitude, the re-sampling procedure (Sect. 3.1) duplicates 30 times each clear sky wind observation at 87 km on a 3 km grid (Fig. 3a, 3d). If clear sky winds were homogeneous over 87 km, this operation would lead to accurate results at a resolution of 3 km, but it is a source of inaccuracies when the sub-grid variability (below 87 km) of clear-sky winds is large. To quantify this error, we use two independent datasets, from an aircraft and from a high resolution model.

First, we use profiles of wind acquired using an airborne 2µm Doppler Wind Lidar (DWL) operated by the German Aerospace Center (DLR) onboard a Falcon aircraft during the AVATAR-T validation campaign of Aeolus. This Lidar has a spatial resolution of 200 m horizontally and 100 meters vertically, extending between the surface and the aircraft which usually flies at about 10 km to 11 km of altitude. To retrieve the horizontal wind, an azimuth scan is applied and takes about 42 s, leading to a horizontal resolution of about 8 km (Witschas et al., 2017, 2022). The systematic error of horizontal wind measurements is estimated to be 0.1 ms⁻¹ and the random error about 1 ms⁻¹. A total of 8250 km was scanned by the aircraft near Cape Verde during the 5 flights we selected. A first selection is made to discard bins with an uncalibrated backscatter superior to 500 (that we estimated a good threshold to discriminate clear and cloudy sky). We first project the wind as if it was observed by Aeolus during its descending orbit and we average the wind vertically to a resolution similar to that of Aeolus of 500 m (5 consecutive bins vertically in a single profile). We then extract from the curtain segments of 500 m vertically x 88 km horizontally (11 consecutive profiles), the closest from Aeolus clear sky observations. A total of 94 independent segments were sampled with 11 consecutive bins with valid wind measurements in clear sky conditions. For each segment, we calculate the standard deviation of the wind within the segment. A standard deviation equals to zero means that there is no horizontal "sub-grid" variability of the wind, and thus, the coarse resolution of Aeolus does not miss any subgrid atmospheric circulation. The higher the standard deviation, the more sub-grid circulations are missed by Aeolus, making the re-sampling of the winds from 87 to 3 km questionable. We observed that in 97 % of the clear sky segments, the standard



330

335

340

345

350



deviation of the wind within the segment is lower than 2 ms⁻¹ and in 83 % of the segments, it is lower than 1 ms⁻¹ (Fig. 4). This stresses out that when re-sampling the clear sky wind from 87 to 3 km, a sub-grid variability of about 1 ms⁻¹ is lost within the clear sky segment.

To get even closer to the actual re-sampling resolution, we used a WRF simulation (more details about this simulation can be found in Ban et al., 2021) over Europe with a horizontal resolution of 3 km in clear sky. The domain is about 1200 km by 1500 km wide and tilted westward by about 8 degrees. This configuration means that the "latitude" axis of the domain is aligned with typical ascending orbit tracks of Aeolus. This allows us to repeat the procedure described above for the 2µm DWL with the WRF simulation. We also vertically average over 500 m but we horizontally average the wind over segments of 87 km (29 consecutive bins). A total of 327 independent segments were sampled with clear sky only. We limited the domain vertically to 10 km to stay consistent with the airborne observations. Despite the finer resolution, the sub-grid variability of the horizontal wind is found to be relatively close to that observed by the DWL with 95 % of the segments having a sub-grid variability of less than 2 ms⁻¹ and 86 % of the segments less than 1 ms⁻¹. When extending the analysis of the WRF simulation up to 18 km (similar to the maximum altitude reached by Aeolus in our dataset, not shown here), the variability of the horizontal wind is even less, with 99 % of the segments having a sub-grid variability inferior to 2 ms⁻¹ and 90 % of the segments less than 1 ms⁻¹. With WRF the conclusions are the same that with the airborne DWL (which is noisy but coarser). Overall, a natural sub-grid variability of about 1 ms⁻¹ is missed by the coarse resolution of Aeolus, making atmospheric circulations of horizontal scale smaller than 87 km and with winds less than 1 ms⁻¹ in clear sky segments non observable. However, it is possible to study circulations at a 3-15 km horizontal scale in cloudy conditions and to compare them to the geographically closest clear sky observations, provided that we increase the uncertainty measurement in clear sky conditions by 1 ms⁻¹ to take account of the non-observed sub-grid variability. Section 4.3 is dedicated to such comparisons at cloud scale.





370

375

380

385

365 Cumulative Distribution Function [9

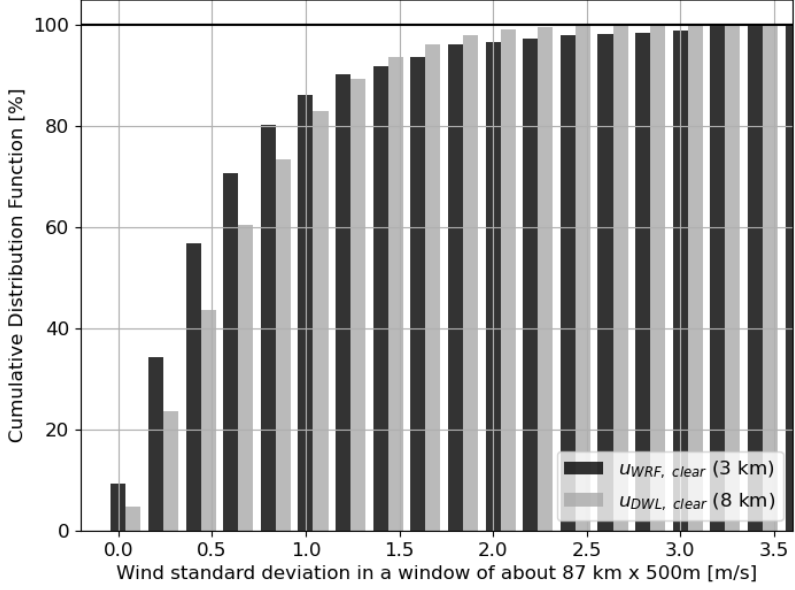


Figure 4: Standard deviation of the wind speed within a segment of about 87 km as observed by the airborne DWL with a horizontal resolution of 8 km and from a the model WRF with a horizontal resolution of 3 km. DWL and WRF wind profiles are averaged vertically to a resolution of 500 m which is the best vertical resolution of Aeolus and close to the vertical re-sampled resolution of our dataset (480 m). The datasets include wind speeds between the surface and 10 km.

3.3 Case study of a tropical cyclone observed with Aeolus

For a general audience, the most famous phenomenon associating clouds and winds is certainly the cyclone. This mesoscale system that develops over warm oceans combines both an opaque cloud cover that can be observed from space (Fig. 5a) and very fast winds around its center. During its lifetime, Aeolus observed multiple cyclones, sometimes crossing them near their center. Figure 5 shows an example of intersection between Aeolus and a tropical cyclone over the Atlantic Ocean during the cyclic season 2020. The wind and cloud curtains are displayed between 20°N and 40°N. Note that Aeolus covers this distance in about 4 minutes, so the curtain represents a snapshot of the scene. The cyclone is localised by the continuous opaque high cloud cover between 20°N and 32°N. This prevents us from actually observing the winds inside the cyclone as the laser typically only penetrates 1 to 2 km below the cloud tops before being fully attenuated. However, Aeolus observes the clear sky winds surrounding the cyclone and typically from the surface to 18 km to altitude. The cross section of the

https://doi.org/10.5194/egusphere-2025-2065 Preprint. Discussion started: 26 May 2025

© Author(s) 2025. CC BY 4.0 License.



EGUsphere Preprint repository

observed clear sky winds (Fig. 5d, but also visible Fig. 5e) reveals the wind shear found where counter-clockwise winds around the cyclone base meet the clockwise winds at the top of the cyclone (within the outflow). This happens at about 8 km of altitude at 25°N and 35°N. The further we look from the cyclone, the higher in altitude the reversal of the wind occurs.

Note that in the paper, we use the convention that eastward winds are positive and westward winds are negative. More

details are given Fig. B1.

The case study visually illustrates how noisy the wind measurements are, especially in clear sky (random error of about 5 ms⁻¹) and to a fewer extent in cloudy sky (random error of 3 ms⁻¹). One should remember that after the high resolution resampling of the winds, a temporal or spatial averaging is necessary to reduce the random error of Aeolus wind

measurements.

This particular case study is also interesting as it encounters a diversity of clouds. We observe shallow cumulus clouds (Fig. 5b) between 20°N and 23°N, with their tops below 3 km and sometimes only occupying a single profile and surrounded by clear sky profiles. This stresses out the importance of performing cloud detection at full horizontal resolution of 3 km. We also observe cirrus clouds, northward of the cyclone, extending from 33°N to 34°N and between 12 and 15 km of altitude.

Along half of its length, this cirrus does not fully attenuate the laser as some clear sky layers can be retrieved below its base.

405

390

395

400





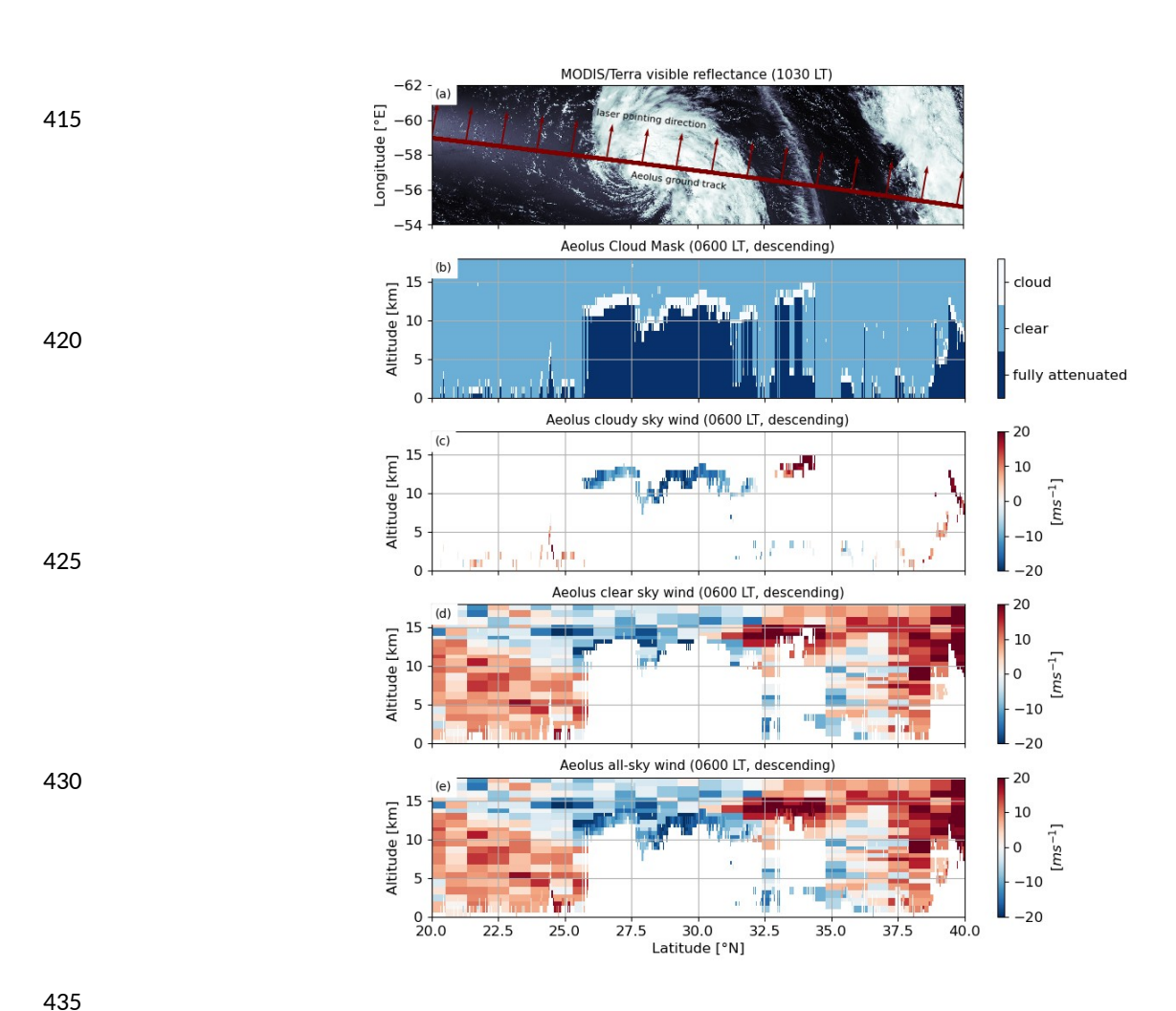


Figure 5: (a) Descending orbit segment in a tropical cyclone over the Atlantic ocean (2020-09-12T09–2020-09-12T11) plotted in red over a MODIS/Terra reflectance image. The red arrows represent the laser pointing direction. (b) Aeolus cloud mask. (c) Aeolus wind in cloudy sky. (d) Aeolus wind in clear sky. (e) Aeolus all-sky wind. In (b), (c), (d) and (e), the resolution of the re-sampled data is 3 km horizontally and 480 m vertically.



450

455

460



4 Results at different scales

In this section, we illustrate analyses with our observations through three examples at different spatial scales: large, regional and cloud scale inferior to 100 km.

4.1 Global-scale circulations observed with Aeolus

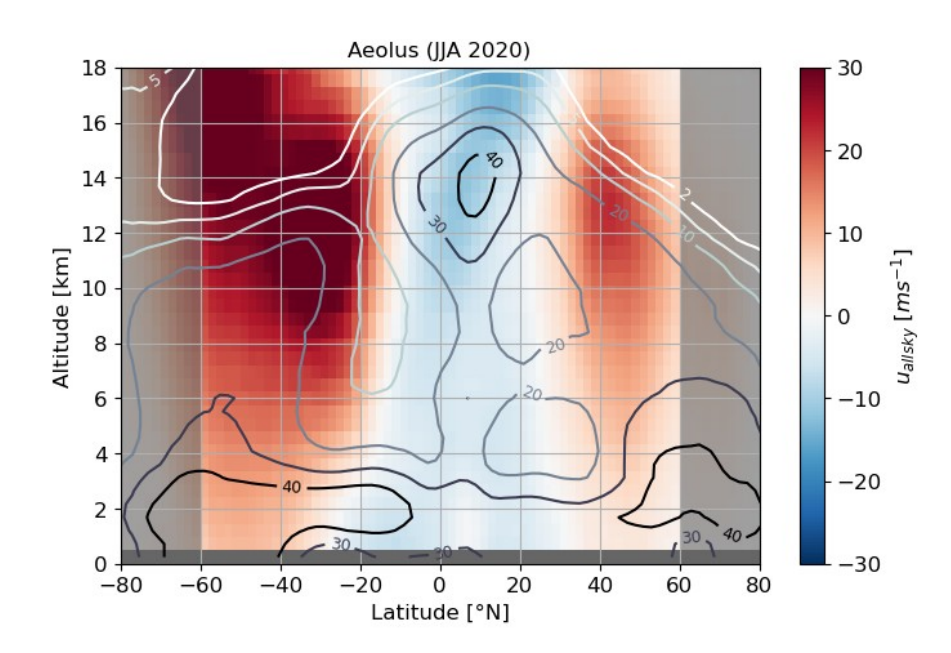


Figure 6: (a) Zonal average of all-sky wind speed profiles. Contours represent the fraction of re-sampled winds retrieved in cloudy sky to the total number of re-sampled winds (clear + cloudy sky winds). Latitudes higher than 60° are shaded as the laser is not pointing in a zonal direction (Fig. 1).

Aeolus observes the main features of the general circulation, like for example the trade winds below 2 km of altitude between 20°S and the equator and from 10°N to 20°N (Fig. 6) and the subtropical jet streams at 30°S and 40°N with their cores located at 12 km of altitude. As this zonal average of wind profiles is calculated from June to August 2020, the polar stratospheric jet is visible around 55°S and 17 km of altitude. Moreover, the speed of the subtropical jet stream in the southern hemisphere is larger than 35 ms⁻¹ due to a large meridional temperature gradient in the winter hemisphere through thermal wind balance, while the northern hemisphere subtropical jet stream only reaches 25 ms⁻¹. This difference between the two hemispheres is also visible on the map of wind shear through the troposphere (Fig. 7), where S_{tropo} is defined as:

$$S_{tropo} = \frac{u_{allsky}(z_2 = 10 \, km) - u_{allsky}(z_1 = 2 \, km)}{(z_2 - z_1)},\tag{3}$$



480

490



The wind shear is here computed between 10 km (within the troposphere between 60° N and 60° S) and 2 km (the typical border between the boundary layer and the free atmosphere), but a similar study can be performed with another choice of altitudes. The wind shear ranges between 1×10^{-3} and 3×10^{-3} s⁻¹ in the northern hemisphere while it largely exceeds 3×10^{-3} s⁻¹ in the southern hemisphere. During boreal summer, the Indian Ocean exhibits eastward surface winds typical of the monsoon circulation and a Tropical Easterly Jet with a core at 16 km of altitude. This results in the strongest negative wind shear, with values below -3×10^{-3} s⁻¹ (wind profile is sheared westward as we go up in altitude). This region is also subject to deep convection (Hemanth Kumar et al., 2015) during this period as well as an important cirrus cloud fraction (Ali et al., 2022). As a result, this is also over the Indian Ocean that Aeolus retrieves the largest proportion of winds in cloudy sky at 10 km of altitude, up to 25 %. Everywhere else in the tropics, between 2 % and 10 % of the winds at 10 km of altitude are retrieved in cloudy sky, the remaining are retrieved in clear sky. Note also that low fractions of cloudy sky winds (vs all sky winds) correspond in the Northern Atlantic and Pacific Oceans, to regions of strong positive shears (wind profile is tilted eastward as we go up in altitude), up to 3×10^{-3} s⁻¹ that are typical of a strongly stratified free troposphere.

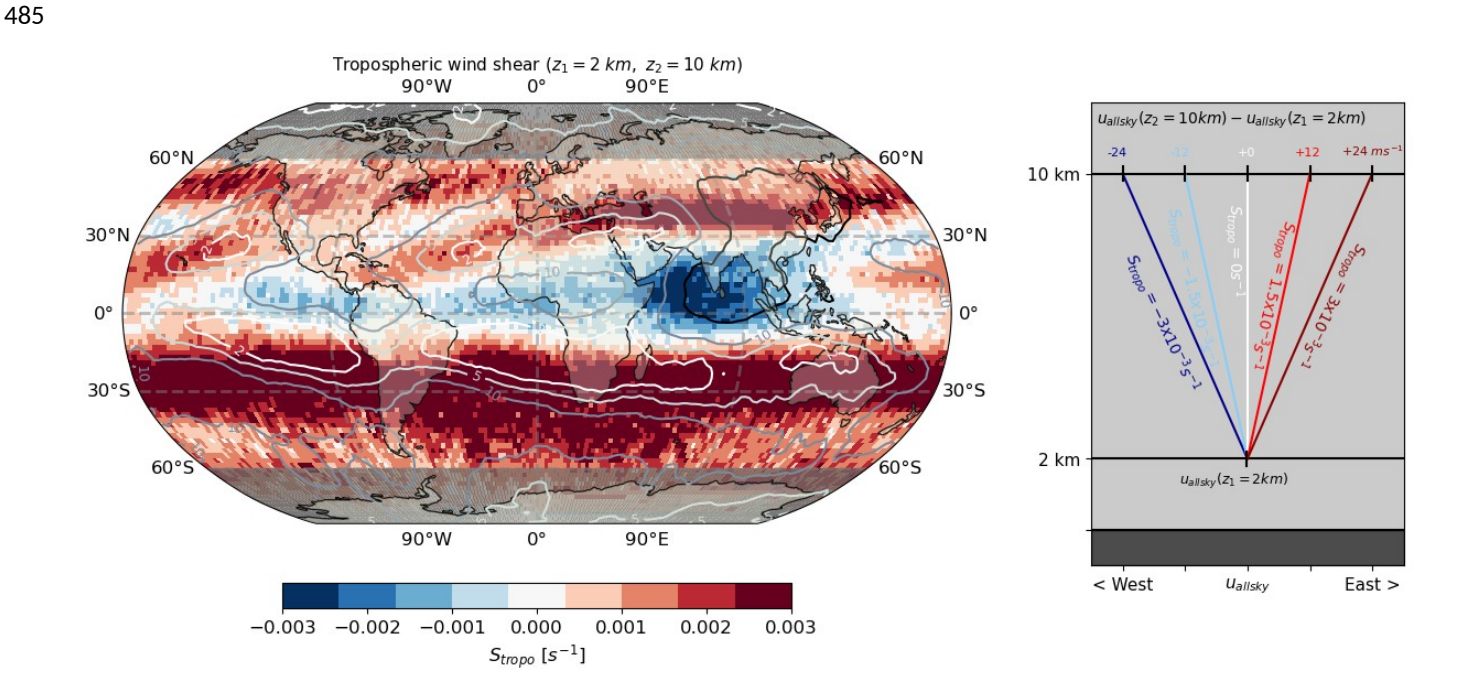


Figure 7: Map of the wind shear S_{allsky} calculated between z_1 =2 km and z_2 =10 km at 2° x 2° from June to August 2020. Contours represent the fraction of re-sampled winds retrieved in cloudy sky at 10 km of altitude to the total number of re-sampled winds (clear + cloudy sky winds) retrieved at 10 km of altitude. Latitudes higher than 60° are shaded as the laser is not pointing in a zonal direction (Fig. 1). Schematic on the right illustrates the link between the colorbar used on the wind shear map on the left and the typical wind profile associated.





4.2 Seasonal changes of clouds and winds over the Indian Ocean

During the months of June-August, we observe a maximum of high cloud fraction over the Indian Ocean (Fig. 8e), as well as a Tropical Easterly Jet (TEJ) that extends from the Tibetan plateau to the Western coast of Africa (Fig. 8f). The core of the TEJ is located at about 16 km of altitude. It is visible on the maps Fig. 8c with westward winds exceeding 30 ms⁻¹. We focused on a small domain located over the Indian Ocean on the Western coast of India and under the influence of the TEJ during summer (black rectangle, Fig. 8a). The domain extent of 20° of longitude ensures that Aeolus crosses it at least twice a day, once ascending and once descending. On the time series of wind profiles (Fig. 8f), the apparition of a westward (negative) wind speed appears in late May and reaches values of above 30 ms⁻¹ within a few days only. The jet subsists until the last week of October before decaying rapidly, giving way to eastward winds (positive values) again. It is worth noting that during the same period of the TEJ, Aeolus captures persisting eastward (positive) winds below 2 to 5 km of altitude associated to the monsoon circulation. Figure 8e displays the daily average profiles of the cloud fraction observed by Aeolus over the same domain. The low cloud fraction is persistent during the entire year and above 30 % during early winter over the cold Arabian sea and during late September. We also notice two minima which correspond to the reversal of boundary layer winds, in late April and late October. The most striking feature is the presence of high clouds above 5 km and up to 16 km, preferentially occurring between June and October, i.e. when the TEJ is the most active. These high clouds are associated to deep convection and to a large increase of cirrus cloud fraction, that is favoured by horizontal transport of moist air originating from convective towers over long distances (Das et al. 2011). Aeolus observations can be of a great help to better understand these interactions between horizontal winds and cirrus formation.

495

500





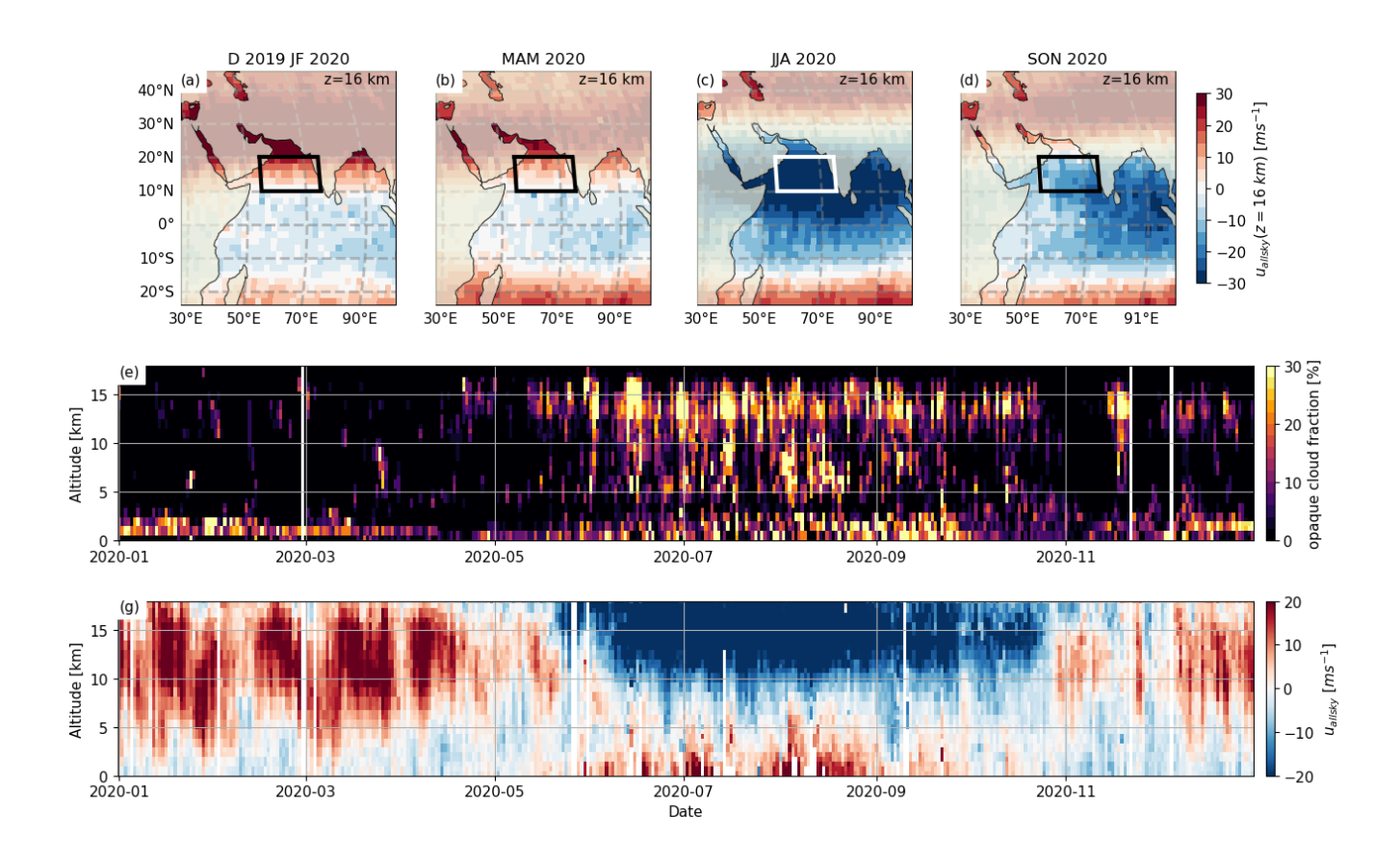


Figure 8: (a) map of the averaged all-sky wind speed u_{allsky} (z=16 km) during the months of December 2019, January and February 2020 (b, c and d) are the same for respectively spring, summer and fall 2020. The rectangle (10°N-20°N, 55°E-75°E) represents a domain selected as it is under the influence of the Tropical Easterly Jet during summer. The time series represent at a daily resolution (e) the average profiles of cloud fraction within the domain and (f) the average profiles of all-sky wind speed within the domain.



525

530

535

540

545

550



4.3 Cloud scale circulations inferior to 100 km

When convection is triggered, the horizontal wind from the sub cloud layer is transported vertically within the cloudy layer, leading to different horizontal wind speeds within the cloudy layer and the surrounding environment at a given vertical level. This phenomenon referred as "Convective Momentum Transport" has been studied using LES (Siebesma et al., 2003), and more recently using airborne measurements (Koning et al., 2022). In this subsection we investigate the ability of Aeolus to significantly retrieve different wind speeds within a cloud and in the clear sky surrounding the cloud.

4.3.1 Is it possible to capture the differences between wind speeds within clouds and their surrounding clear sky at the resolution of Aeolus?

To test the feasibility of significantly observing different wind speeds within clouds and their surroundings with Aeolus, we first used lidar data measured with a Falcon flight during the AVATAR-T campaign. Figure 9 displays an example of cumulus clouds forming near Cape Verde and overflown by the DLR Falcon. We first projected the zonal and meridional components of the wind as if Aeolus was observing the scene during its descending orbit. This results in profiles of upwL, allsky at 100 m vertical resolution and 8 km horizontal resolution. We then further averaged the two upw. allsky profiles encompassing the edge of the cloud between 1284 and 1300 km along flight and performed a sliding average vertically of 500 m, to replicate the original vertical and horizontal resolutions of Aeolus winds. We averaged the clear sky wind profiles on the left edge of the cloud, between 1210 and 1280 km along flight, to simulate as well as possible a clear sky wind profile viewed from Aeolus. We performed a sliding average vertically of 500 m. We see that the clear and cloudy wind profiles are not significantly different below the cloudy layer with u_{DWL, allsky} of about -2 ms⁻¹. The clear sky wind profile is tilted westward and reaches about -5.5 ms⁻¹ at 3 km of altitude. Meanwhile, within the cloudy layer, as air masses from the surface are carried upward within the cloud, the wind decelerates to about -1 ms⁻¹ at 1.6 km of altitude. At this altitude, the difference between the clear sky wind and cloudy sky winds is the largest and reaches 3 ms⁻¹. Note that between the Cloud Base Height (CBH = 1.3 km) and the Cloud Top Height (CTH = 1.9 km), the wind shear within the cloud, about $1 \times 10^{-3} \text{ s}^{-1}$, is lower than in clear sky conditions within the same layers, about 3x10⁻³ s⁻¹. Above the cloud top, where the convective momentum transport is not efficient, cloudy and clear sky wind profiles join again at 2.5 km of altitude. Between the cloud top and 2.5 km, as the wind just above the cloud top experiences drag from the cloud top, the wind shear is negative and maximum in absolute value just above the cloud top, while the clear sky wind profile is almost not sheared

The case study presented in Figure 9 shows that even at the coarse vertical and horizontal resolutions of Aeolus, it is possible to capture significantly different wind speeds within clouds and within their surroundings in shallow convection. This finding encourages us to search for evidences of convective momentum transport in our Aeolus dataset.





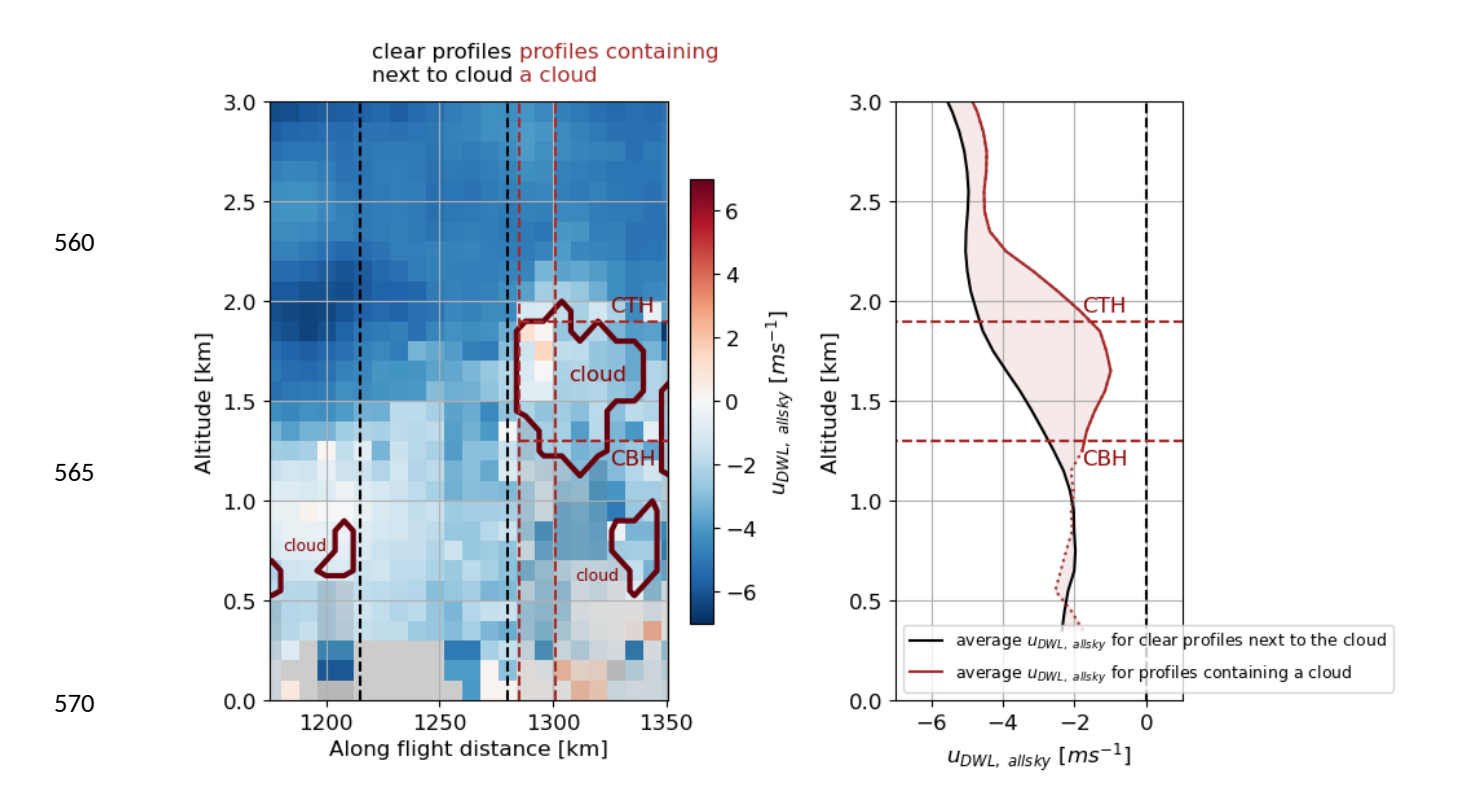


Figure 9: (a) AVATAR-T flight segment with horizontal wind along Aeolus laser pointing direction. The clouds are represented with solid red contours. Vertical red dashed lines represent the horizontal extent of the profiles encompassing a cloud while vertical black dashed lines represent the horizontal extent of clear sky profiles next to the clouds. Horizontal red dashed lines mark the average Cloud Base Height (CBH) and Cloud Top Height (CTH) for the profiles encompassing a cloud. (b) The profiles encompassing a cloud are averaged horizontally as if Aeolus saw them and then vertically at a resolution of 500 m (red curve). The same process is done for clear sky profiles next to the cloud (black curve).



590

595

610

615



4.3.2 Differences between wind speed within clouds and their surrounding clear sky with Aeolus

In order to study wind speed differences of only a few ms⁻¹, it is necessary to reduce the random error and therefore average a large number of wind profiles. We chose to split the study within regions exhibiting different types of clouds and different large-scale circulations. A map of the regions used is given in supplementary material (Fig. B2). The first region is dominated by Stratocumulus decks sometimes transitioning to Cumulus clouds (TrSc) and the second region is dominated by Cumulus clouds (Cu) (McCoy et al., 2017; Qu et al., 2015). These two regions are found above oceans and usually under the subtropical jet streams. The Indian Ocean is the third region, thermodynamically more unstable and prone to deep convection, it is also crossed by the Tropical Easterly Jet during boreal summer. The boundaries of this region are adapted from the INDian Ocean EXperiment (INDOEX, Mitra, 2004) in order not to overlap other boxes. Finally we choose a fourth region over the Pacific Ocean and between the latitudes of 10°S and the equator, referred below as the Pacific warm pool region (WP).

Within each region, we identify profiles containing adjacent cloudy layers in the vertical direction and that are at least 2 km thick in total, typically associated to convective clouds (more details are given in Fig. B6). We record the cloudy wind speed observed in the uppermost cloudy layer (noted ucloud_up) as well as its altitude, and the cloudy wind speed 2 km below the uppermost cloudy layer (noted ucloud_down). We compute the wind shear between these two layers distant of 2 km (noted Scloud). In the same orbit, among the surrounding profiles, we look for the closest profile located at a distance shorter than 100 km that exhibits clear sky winds everywhere in this 2 km thick layer. We record the clear sky wind within this profile (noted uclear_surrounding_cloud_up) at the same altitude as the uppermost cloudy layer. We also record the clear sky wind speed (noted uclear_surrounding_cloud_down) 2 km under uclear_surrounding_cloud_up, coming from the same profile. We compute the clear sky wind shear in the surrounding of the cloud (noted Sclear_surrounding_cloud). Each cloud and its environment are therefore associated to a group of six variables including four wind speeds and two wind shears.

We average cloudy wind speeds observed in the uppermost cloudy layer (u_{cloud_up}) within each region, and at each altitude, to obtain an average profile of u_{cloud_up} for each region. The same processing is performed for the five remaining variables. This averaging procedure reduces the random error by a factor $N^{1/2}$ where N is the number of independent groups of variables within a region and at a specific altitude. For each region and at each altitude, the number of groups exceeds 100, reducing the average $u_{cloud_up}(z)$ and $u_{cloud_down}(z)$ random error to below 0.3 ms⁻¹ and $u_{clear_surrounding_cloud_up}(z)$ and $u_{clear_surrounding_cloud_down}(z)$ to 0.6 ms⁻¹. Above 8 km of altitude, the number of groups ranges between 1000 and 5000 in each region and at each altitude, further reducing the average $u_{cloud_up}(z)$ and $u_{cloud_down}(z)$ random error to below 0.1 ms⁻¹ and $u_{clear_surrounding_cloud_up}(z)$ and $u_{clear_surrounding_cloud_up}(z)$ to 0.2 ms⁻¹. The random error is thus smaller than the typical horizontal wind speed difference



620

625

630

635

640

645



between the uppermost cloudy layer $u_{cloud_up}(z)$ and its clear sky surrounding $u_{clear_surrounding_cloud_up}(z)$, which was estimated to 3 ms⁻¹ in the airborne case study (Fig. 9) and documented to be several ms⁻¹ generally.

Figure 10a shows the average profile of $u_{cloud_up}(z)$ and the average profile of $u_{clear_surrounding_cloud_up}(z)$ for the different regions. Within a single region, each pair of profiles shows the typical shape of the wind speed profile. TrSc and Cu profiles first show an eastward acceleration from the surface to the core of the subtropical jet stream at about 12 km of altitude. Within this altitude range, the average wind shears within cloudy layers (Scloud) and in the surrounding clear sky environment $(S_{clear_surrounding_cloud})$ are positive (Fig. 10b). We find that for both TrSc and Cu, between 3 and 12 km of altitude, $u_{cloud_up}(z)$ is eastward and 1 to 3 ms $^{-1}$ slower (statistically significant) than its paired $u_{clear_surrounding_cloud_up}(z)$ at the same altitude. We also note that average wind shear within the cloud $S_{cloud}(z)$ is about $1x10^{-3}$ to $2x10^{-3}$ s⁻¹. This is about two times lower than the one observed in the clear sky surrounding environment $S_{clear_surrounding_cloud}(z)$, which ranges between $1x10^{-3}$ and $3x10^{-3}$ s⁻¹. Above the jet stream core located at 12 km, the wind profile is tilted westward as it goes up in altitude (negative wind shear) and $u_{cloud_up}(z)$ becomes 1 ms⁻¹ faster to the east than its paired $u_{clear_surrounding_cloud_up}(z)$. Over the Indian Ocean, we observe eastward (positive) ucloud_up(z) and uclear_surrounding_cloud_up(z) between 3 and 10 km of altitude. Within this altitude range, the wind shear within clouds is almost null while the wind shear in clear sky surrounding the clouds is positive but weak at about 1x10⁻³ s⁻¹. $u_{clear_surrounding_cloud_up}(z)$ are between 0 and 1 ms⁻¹ faster than $u_{cloud_up}(z)$ to the East below 10 km of altitude, and more than 1 ms⁻¹ faster than ucloud up(z) at about 7 km of altitude (statistically significant). Above 10 km of altitude, still in the Indian Ocean, the observed wind speeds change direction and become westward, with $u_{clear surrounding cloud up}(z)$ 1 to 3 ms⁻¹ faster than $u_{cloud up}(z)$ and the observed wind shears become negative, reaching -3x10⁻³ s⁻¹ in clear and cloudy skies. At almost each altitude above 10 km, the wind shear is stronger in the clear sky surrounding the clouds than in the clouds themselves and this difference is statistically significant. Above the Warm Pool, the differences between the cloudy wind shear and the surrounding clear sky wind shear are below $1x10^{-3}$ s⁻¹ and the wind shears themselves are weak, between 0 and $-1x10^{-3}$ s⁻¹ throughout the entire profile, except above 14 km of altitude, where $S_{clear surrounding cloud}$ reaches $2x10^{-3}$ s⁻¹ and $u_{clear surrounding cloud up}(z)$ is 1 ms⁻¹ faster to the west than $u_{cloud\ up}(z)$.

Over the stratocumulus and cumulus dominated regions, the wind shear within clouds is systematically smaller than the wind shear in the clear sky surrounding the clouds, up to 2 times at some altitudes, and this difference is statistically significant. We also observed that in these three regions, the differences between $u_{cloud_up}(z)$ and $u_{clear_surrounding_cloud_up}(z)$ can reach above 3 ms⁻¹, particularly at altitudes where the wind shear $S_{clear_surrounding_cloud}$ is the largest.





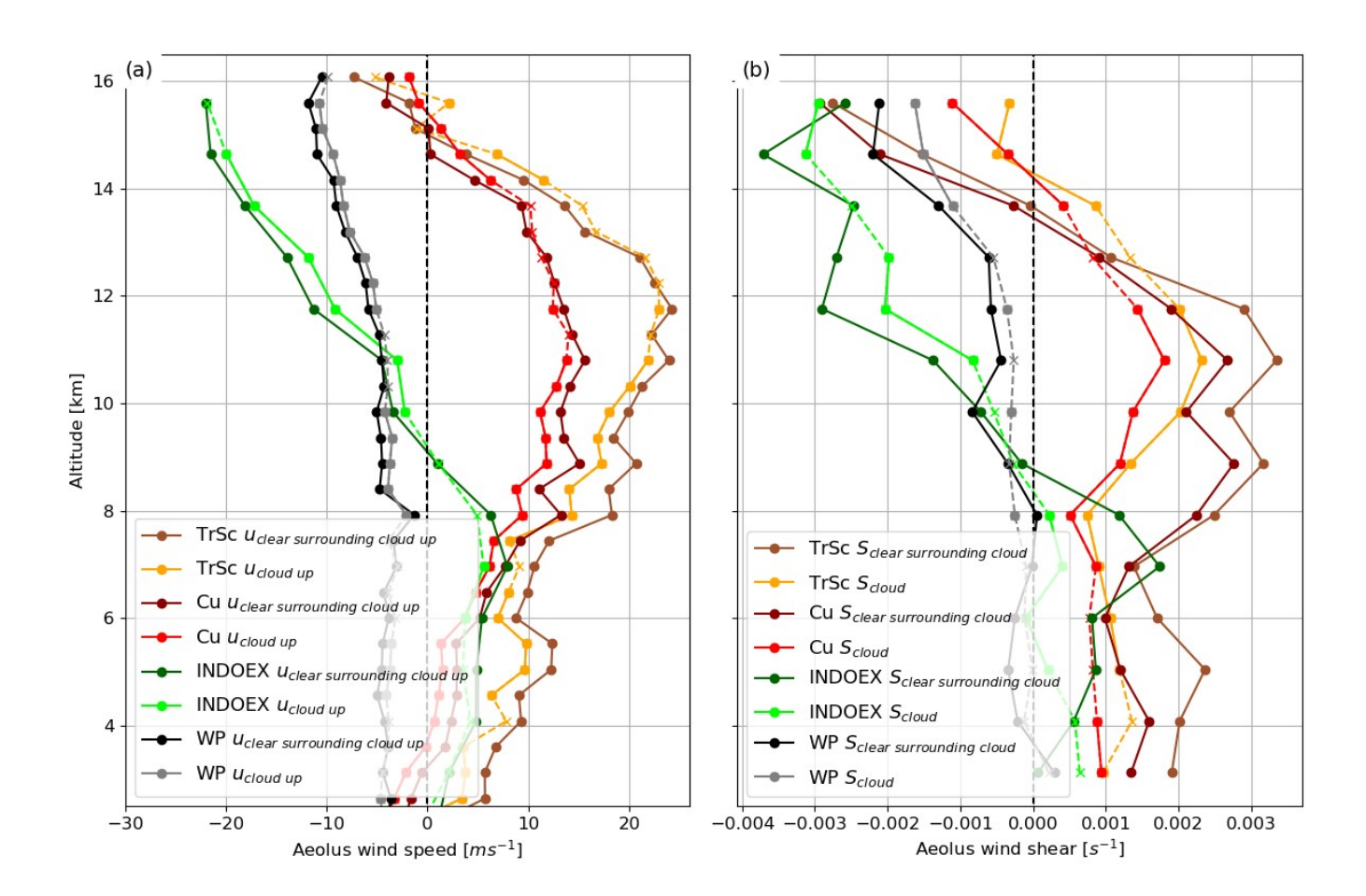


Figure 10: (a) Average wind speed profiles retrieved within the uppermost cloudy layer $u_{cloud\ up}(z)$ and average of the closest clear sky winds $u_{clear\ surrounding\ cloud\ up}(z)$ observed by Aeolus over four regions with different thermodynamics during the year 2020. Each layer of the cloudy wind profiles are plotted with solid lines when they are significantly different from the clear sky wind at the same altitude (p-value < 0.05) otherwise the line is dashed. (b) is the same as (a) but with the wind shear at each altitude z is defined as the difference between the wind two layers above z (960 m above z) and the wind two layers below z (960m under z).

4.3.3 First observations of Convective Momentum Transport with Aeolus

One of the striking conclusions derived from the analysis of Fig. 10 is the systematic correlation between the sign of the $u_{cloud_up}(z) - u_{clear_surrounding_cloud_up}(z)$ and the sign of the wind shear in the surroundings of clouds, $S_{clear_surrounding_cloud}(z)$, at each altitude. In fact, the differences $u_{cloud_up}(z) - u_{clear_surrounding_cloud_up}(z)$ show a quasi linear relationship (Fig. 11) with the values of $S_{clear_surrounding_cloud}(z)$ for the TrSc, Cu and the INDOEX regions with correlation coefficients of respectively R=0.89, R=0.93 and R=0.68. Our results are very consistent with those obtained with a Cloud Resolving Model by Grubisic and Moncrieff





(2000), who also show a weaker horizontal wind in the updraft (analogous to our cloudy sky) than in the downdraft region (analogous to the clear sky surrounding the cloud) in positive wind shear conditions, and a larger difference between updraft and downdraft winds when the wind shear increases. This result suggests that for strongly sheared regions, Aeolus, at its coarse resolution can observe significant differences between the winds in the uppermost layer of convective clouds and their clear sky surrounding. And these differences correlate well with the wind shear in the surrounding of clouds. This is in line with the K-theory, that stipulates the averaged wind perturbations in a turbulent fluid are proportional to the averaged wind shears. Regarding the Pacific Warm Pool, as expected, the wind profile is on average less sheared than in the other regions with an average $u_{clear_surrounding_cloud_up}(z)$ of about -5 ms⁻¹ near the surface and -10 ms⁻¹ at 16 km of altitude and differences between $u_{cloud_up}(z)$ and $u_{clear_surrounding_cloud_up}(z)$ barely exceed typically 1 ms⁻¹.

670

675

680

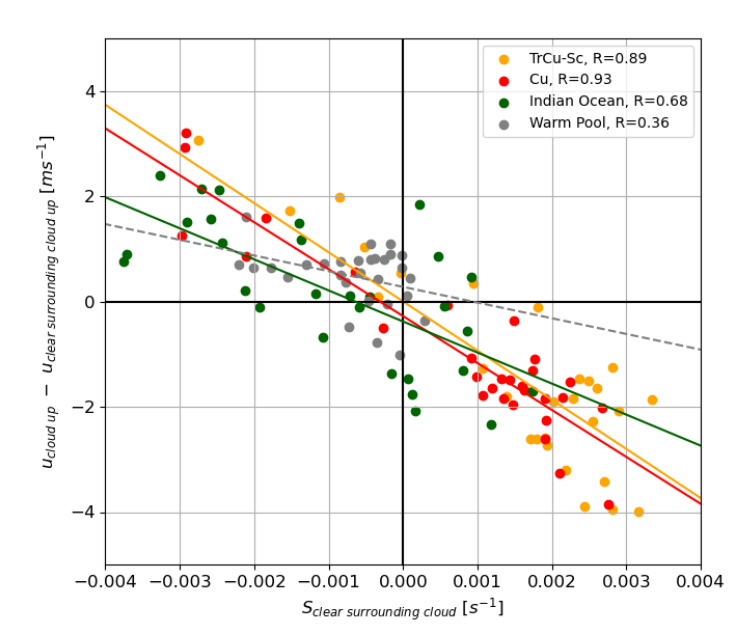


Figure 11: Correlation between the averaged values of the wind shear in the clear sky surrounding the cloud $S_{clear_surrounding_cloud}(z)$ and the wind speed perturbation associated to the cloud presence, $u_{cloud}(z) - u_{clear_surrounding_cloud}(z)$ for each region. Each point represents an altitude level.



695

700



5 Summary and future work

The observations presented in this paper display for the first time merged cloud vertical profiles and vertical profiles of horizontal wind at global-scale. We constructed cloud profiles at 3 km of horizontal resolution and re-sampled vertically at 480 m, using Aeolus L1A uncalibrated backscatter data coming from the detector of the Mie channel only. Corrections were applied to compensate for the varying vertical resolution and optical properties of the detector, the lack of the cross-polar backscattered signal as well as the increasing number of hot pixels during the mission. Globally, the obtained cloud fraction profiles showed a good agreement with CALIPSO-GOCCP cloud profiles with an R² of 0.79, Pearson correlation of 0.86 and local cloud fraction differences below 3 % in most of the entire free troposphere. Using this cloud detection, we re-sampled the already calibrated and validated L2B Aeolus winds on a curtain of 3 km of horizontal resolution and 480 m of vertical resolution. We assessed that Aeolus re-sampled clear sky winds at 3 km are representative of the actual wind at 3 km of resolution, (with differences below 1 ms⁻¹ in 84% of the cases), based on airborne Doppler Wind Lidar data and a regional weather model simulation at high spatial resolution.

To highlight the potential of this dataset, we showed unique global, perfectly co-located, direct observations of cloud and wind profiles within the entire troposphere during boreal summer 2020. Unsurprisingly, the main zonal global-scale circulations are well captured by Aeolus. This includes the almost cloud-free subtropical and tropical jet streams as well as the tropical tropopause circulation. This opens perspectives of exploring deeper the shift in intensity and position of the subtropical jet stream induced by the cloud radiative effect, particularly in regions with a low number of in-situ observations. We also found that over the Northern Atlantic and Pacific Oceans, regions with the strongest wind shears between 2 and 10 km of altitude (> 3x10⁻³ s⁻¹) are the less cloudy at 10 km of altitude (cloud fraction < 2 %). Over the Indian Ocean, we observed low altitude cloud fractions of about 30 % in January that decrease until April 2020 and then increase again while the Monsoon onsets (June to September 2020). In the upper troposphere, when the Tropical Easterly Jet starts (early June), winds in its core quickly reach speeds of above 40 ms⁻¹ and high cloud fractions suddenly increase at the same time, exceeding 30 %.

Finally, regarding circulations at cloud scales inferior to 100 km, we analysed the averaged wind speed differences between the uppermost layer of convective clouds and the surrounding clear sky. After confirming that these wind speed differences can be observed at the resolution of Aeolus observations (using an airborne case study averaged at the resolution of Aeolus), we split the study in regions having different large scale circulations. Over regions dominated by Stratocumulus and Cumulus clouds, convective motions induce large wind speed differences between the uppermost cloudy layer and their clear sky environment, exceeding 3 ms⁻¹ at some altitudes. We finally showed that these wind speed differences correlate with the wind shear in the clear sky surrounding the cloud. This correlation is particularly strong with R=0.93 over Cumulus and





R=0.89 over Stratocumulus dominated regions. This is a direct evidence that horizontal momentum transported by convective motions can be observed by Aeolus.

These few applications show the potential of this new observations for studying wind-cloud interactions at different horizontal scales, extending from 3 km to the global scale. In the near future we plan to focus on the correlation between cirrus covers and the strengthening of horizontal winds (Das et al., 2011), and on the interactions between the cloud radiative effect and jet stream shifting (Voigt et al., 2021). The case study on the tropical cyclone also opens perspectives to study how the wind shear contributes in the organization of shallow convection from random patterns to clusters (Mieslinger et al., 2019; Bony et al., 2020) and sometimes mesoscale convective systems (Houze 2004; Schumacher and Rasmussen, 2020; Abramian et al., 2022).

735

740





Appendix A: Schematics of the signal received on the detector of the Mie channel

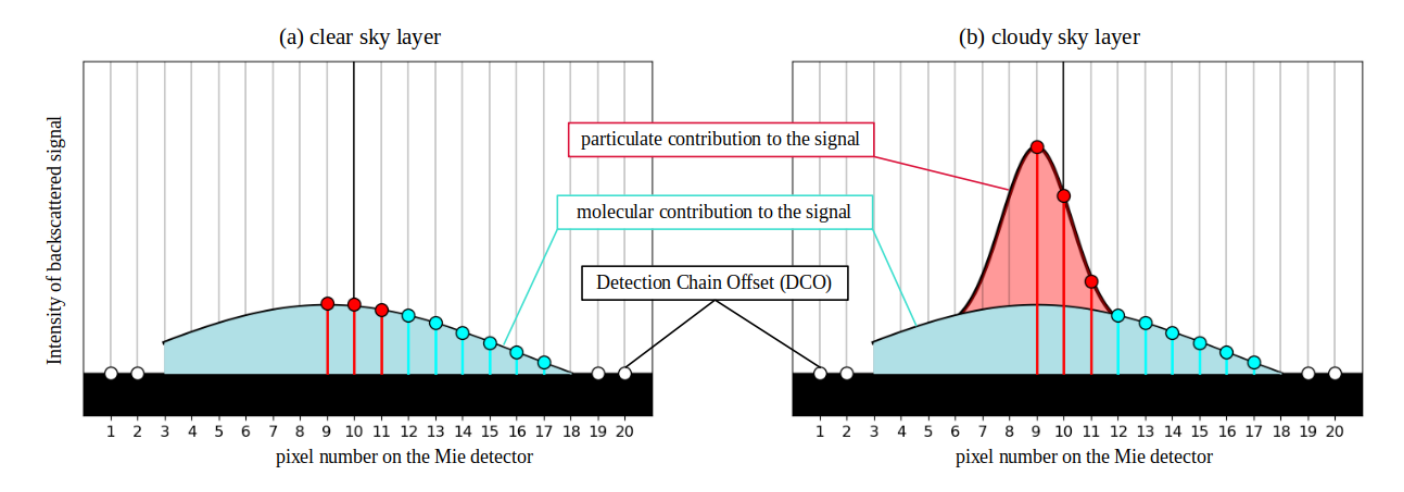


Figure A1. Schematics of the signal received on the detector of the Mie channel (a) in the case of a clear sky layer and (b) in the case of a cloudy layer. Note that these are not at scale and in the case of a cloudy scene, the particulate backscattered signal peak is much larger compared to the molecular backscattered spectrum.

On Fig. A1, we display the intensity of the backscattered signal retrieved on each of the 16 central pixels (pixels 3-16) of the Mie channel detector in a single profile at one altitude level. Note that the pixels 1, 2, 19 and 20 only store information about the Detection Chain Offset (DCO), and the average value stored on these four pixels is averaged and subtracted to the backscattered signal. In the case of Aeolus, a fraction of the molecular backscattered signal is retrieved on the Mie detector and shown in blue. The intensity of this molecular signal essentially depends on the molecular density. The center of the distribution, contains information about both the molecular and particulate backscattered signals. The red part is only due to the presence of aerosols such as cloud droplets or ice particles which are much slower than individual molecules. Therefore, the intensity of the red peak at the center increases in the presence of a cloud as shown in Fig. A1b and is nonexistent or small in the absence of clouds as shown in Fig. A1a.

In the case of Fig. A1, the signal retrieved in the pixels corresponding to the peak of the backscattered signal is found on pixel 9 (left part of the Mie channel detector), therefore the value of the signal stored in pixel 9 and in the two neighboring pixels on its right (pixels 10 and 11) are summed and noted $I_{part}(z_{L1A})$ in this paper, z_{L1A} being the altitude of the center of a layer in a L1A profile. The signal retrieved in the six following pixels to the right of pixel 11 (pixels 12-17) are summed and correspond to the molecular backscatter, called $I_{mol}(z_{L1A})$. Although the molecular backscattered signal (in arbitrary unit) in this approach does not represent the actual molecular backscatter (in m^{-1} sr⁻¹), it is proportional to it, enabling us to use the difference between $I_{part}(z_{L1A})$ and $I_{mol}(z_{L1A})$ to determine the cloud mask.

755

760



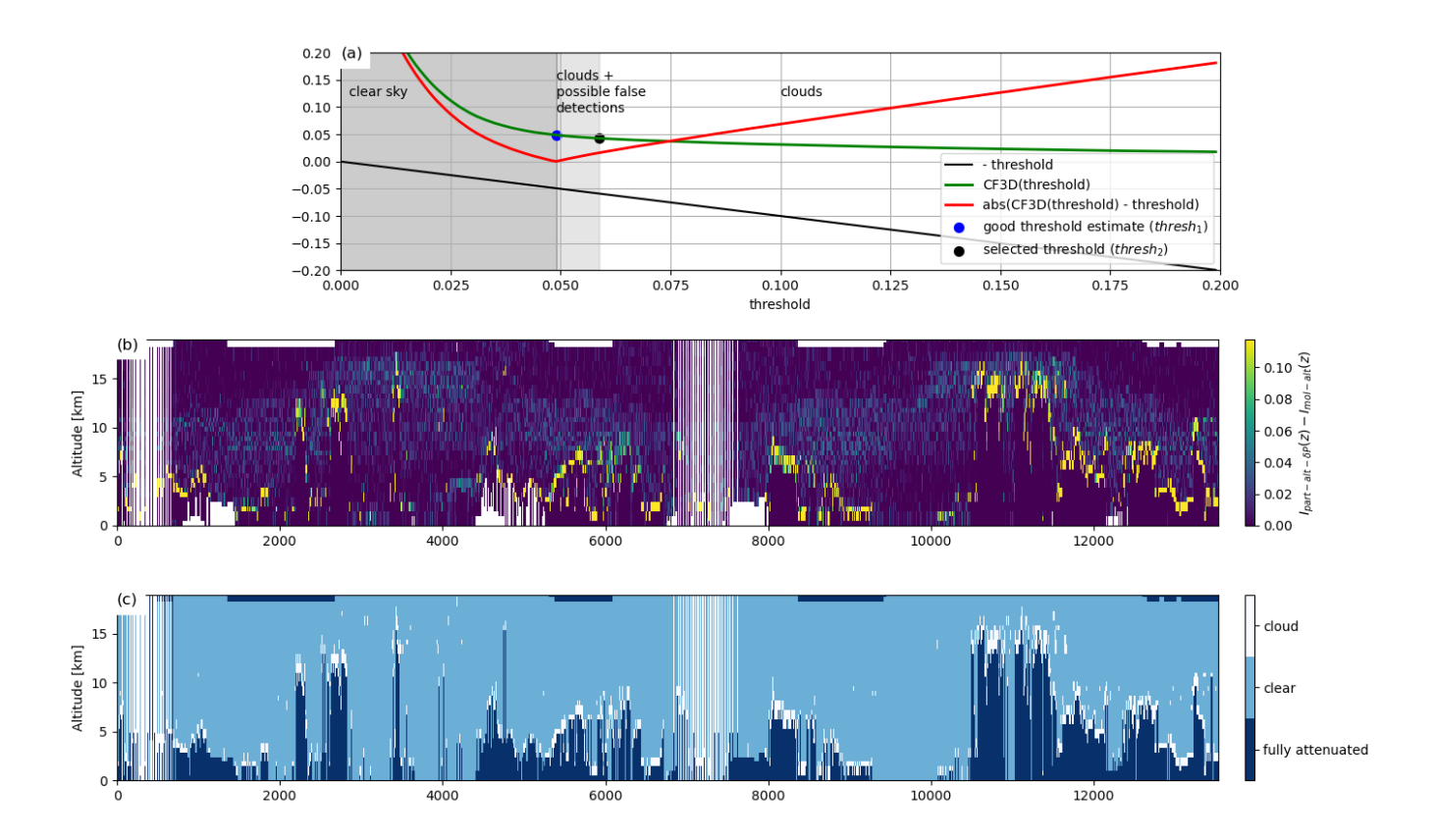


Figure A2. (a) Cloud fraction (CF3D) retrieved depending on the applied cloud detection threshold (green curve), cloud detection threshold (thresh₁, blue dot) and selected cloud detection threshold (thresh₂, black dot) for the orbit 2020-09-12T09-2020-09-12T11 (same as Fig. 5). (b) Cross section of $I_{part-alt-\delta P}(z) - I_{mol-alt}(z)$ for the same orbit and (c) the resulting cloud mask.

For each profile, a layer is declared cloudy when and $I_{part-alt-\delta P}(z) - I_{mol-alt}(z)$ exceeds a certain threshold. We found that from an orbit to the other, the distributions of particulate and molecular backscatters fluctuate. We suggest that a good way to find the cloud detection threshold on $I_{part-alt-\delta P}(z) - I_{mol-alt}(z)$ for each orbit, is to compute the cloud fraction obtained for various thresholds on $I_{part-alt-\delta P}(z) - I_{mol-alt}(z)$, ranging from 0.01 to 0.20 (arbitrary units). The cloud fractions decrease quickly for low values of $I_{part-alt-\delta P}(z) - I_{mol-alt}(z)$, which correspond to the clear sky and Poisson-distributed noise and then a slower decrease, which corresponds to the larger particulate backscatters associated with clouds. A first good estimate of the cloud detection threshold (named thresh₁) is found when abs(CF3D(threshold) – threshold) is minimum. We noticed that thresh₁ still gives false cloud detections, so we consider thresh₂ = 1.2 * thresh₁ to be the ideal threshold to avoid false cloud detections.

780





Appendix B: Complements relative to the dynamic variables estimates

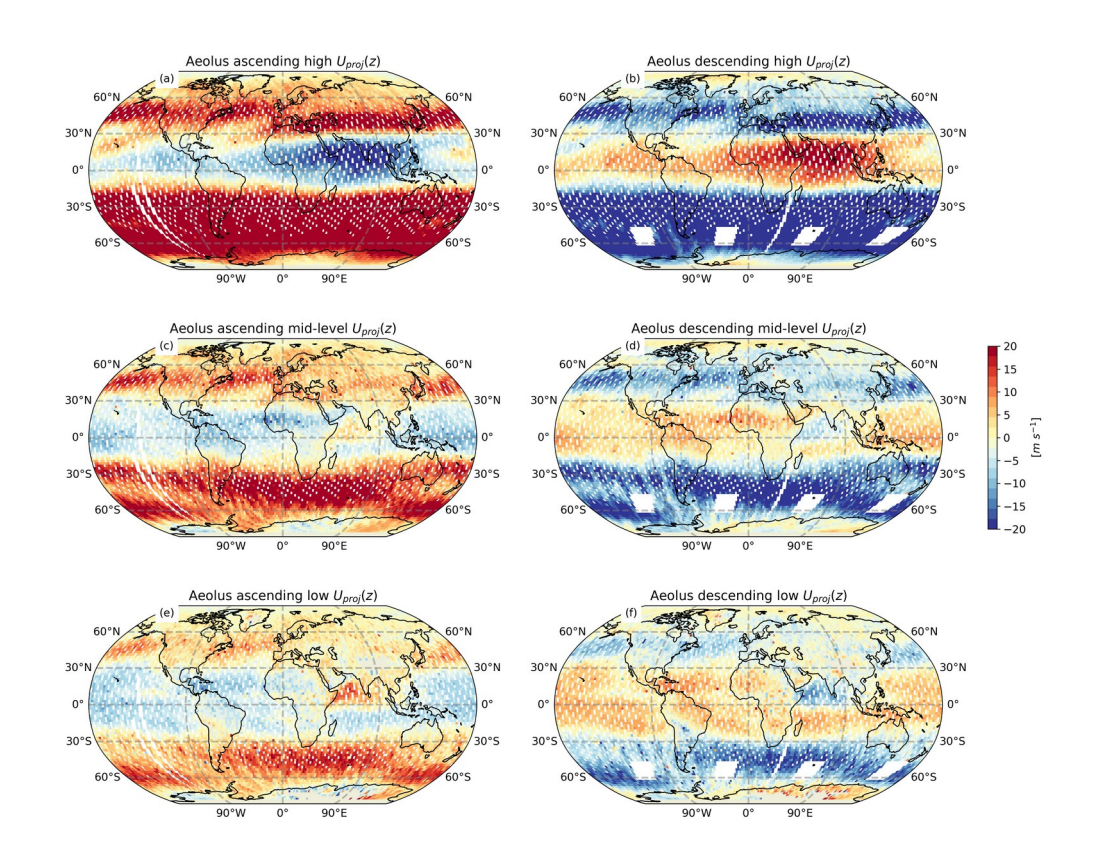


Figure B1: Global maps of all-sky winds (a) above 6.5 km, (c) between 3.2 and 6.5 km, (e) between the surface and 3.2 km for 1800 LT ascending orbits between Jun–Aug 2020. (b), (d) and (f) are the same but for 0600 LT descending orbits, note how the winds for ascending orbits resemble to zonal winds while

Figure B1 illustrates that winds observed during ascending and descending passes are near opposite and a change in the sign of the descending wind gives a good approximation of the zonal wind, especially within the latitude range 60°S-60°N. Indeed, differences exist between the wind observed at 0600 LT and 1800 LT and can be explain by a diurnal cycle of the wind and differences in the laser pointing direction (line-of-sight, Fig. 1). It is possible to estimate zonal and meridional winds from Aeolus but these require making hypothesis about the wind direction or averaging successive ascending and descending orbits. Zonal wind retrievals are detailed in Krisch et al., 2022





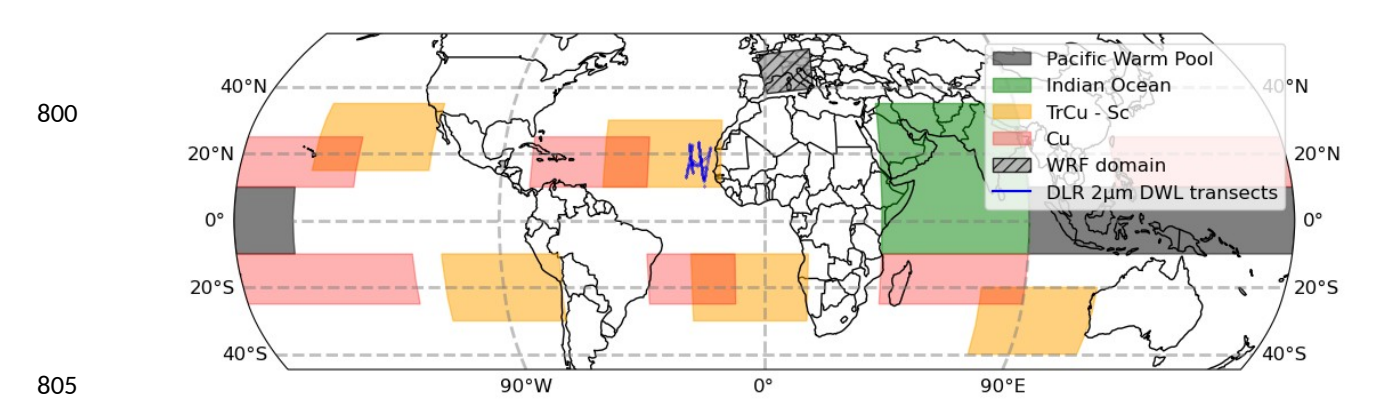


Figure B2: Map of the different regions for CMT studies. Stratocumulus transitioning (orange) Cumulus (red), INDOEX (green) and Pacific Warm Pool (black). The WRF domain is also shown (grey hatched) as well as the transects realised by the DLR Falcon during AVATAR-T (blue).

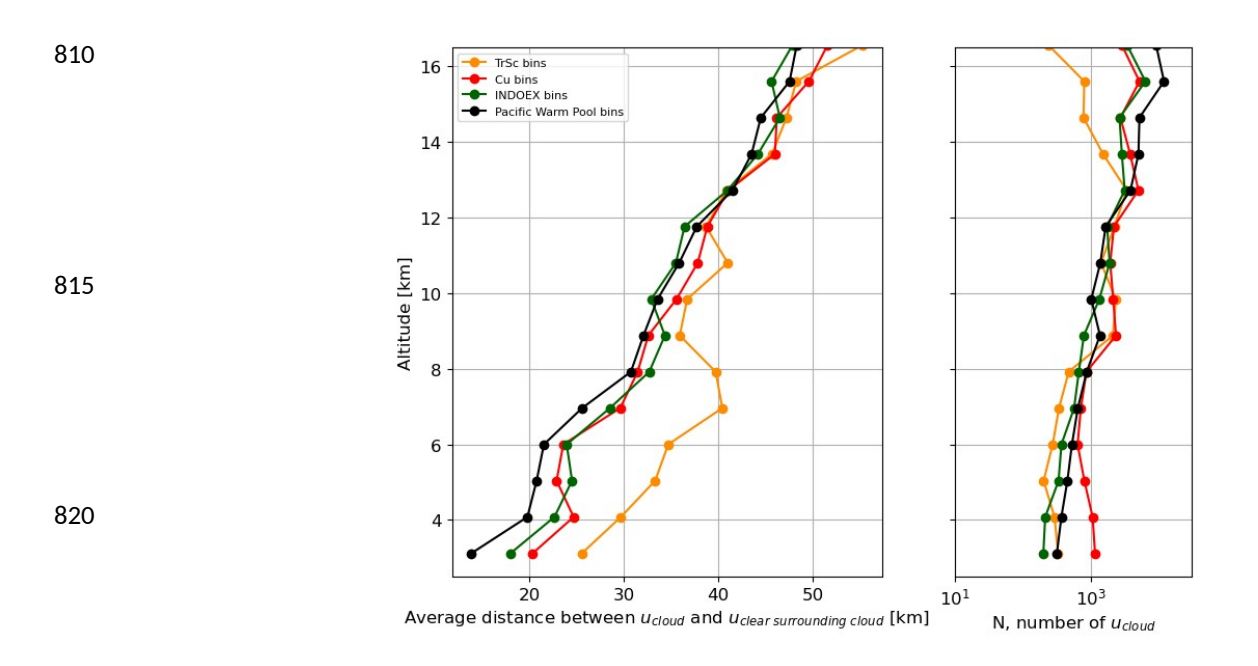


Figure B3: Average distance between pairs of $u_{cloud}(z)$ and $u_{clear_surrounding_cloud}(z)$. All pairs separated by a distance of over 100 km were discarded. (b) occurrences of pairs at each altitude level.





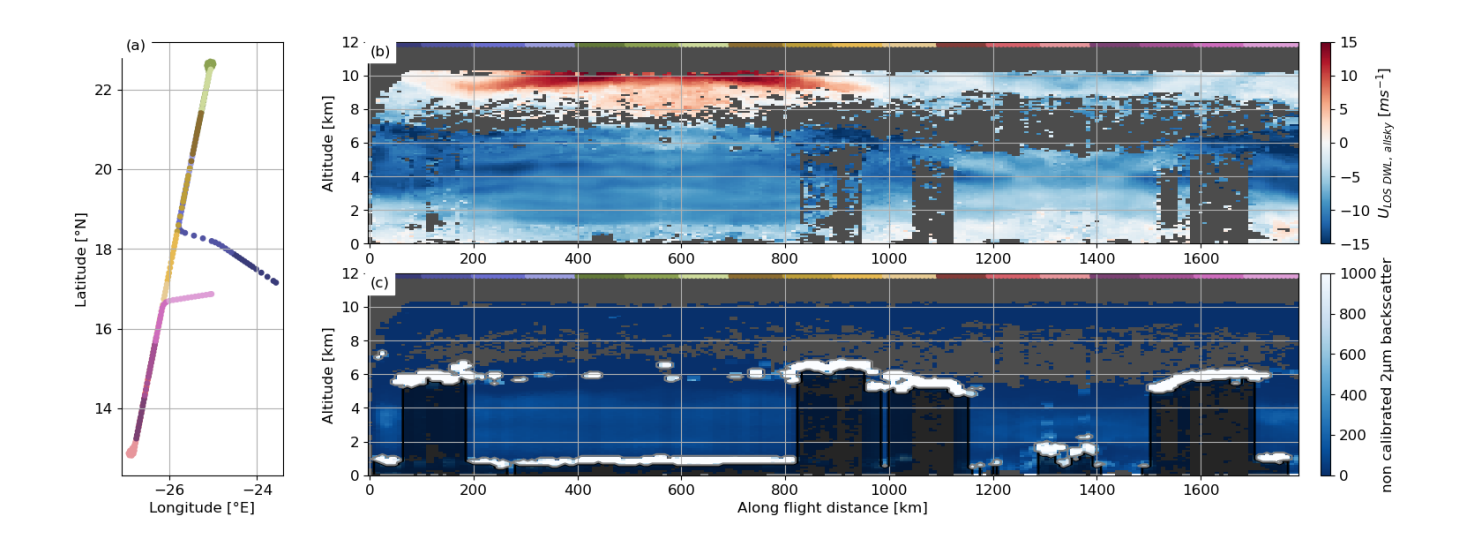


Figure B4: (a) position of airborne LIDAR profiles during AVATAR-T Flight (2021-09-08, same as Fig. 9) over Cape Verde (b) horizontal wind projected along Aeolus line-of-sight ($U_{LOS,\,DWL}$) at a horizontal resolution of 8 km and vertical resolution of 100 m. and (c) uncalibrated 2 μ m backscatter with clouds contoured (grey) and the sub-cloud layers shaded (black). We estimated that uncalibrated 2 μ m backscatter exceeding 500 is associated with clouds.

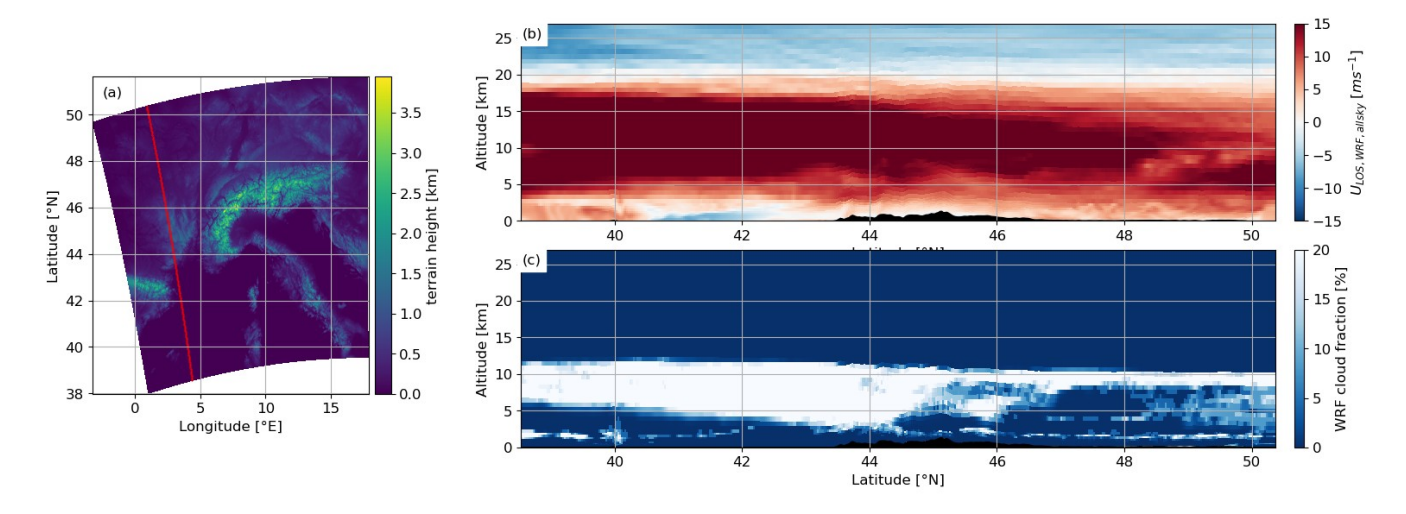


Figure B5: (a) terrain height of WRF simulation, the red curve corresponds to a theoretical orbit track of Aeolus. (b) Horizontal wind projected along Aeolus line-of-sight (U_{LOS, WRF}) at a horizontal resolution of 3 km and (c) the corresponding cloud mask



870

875



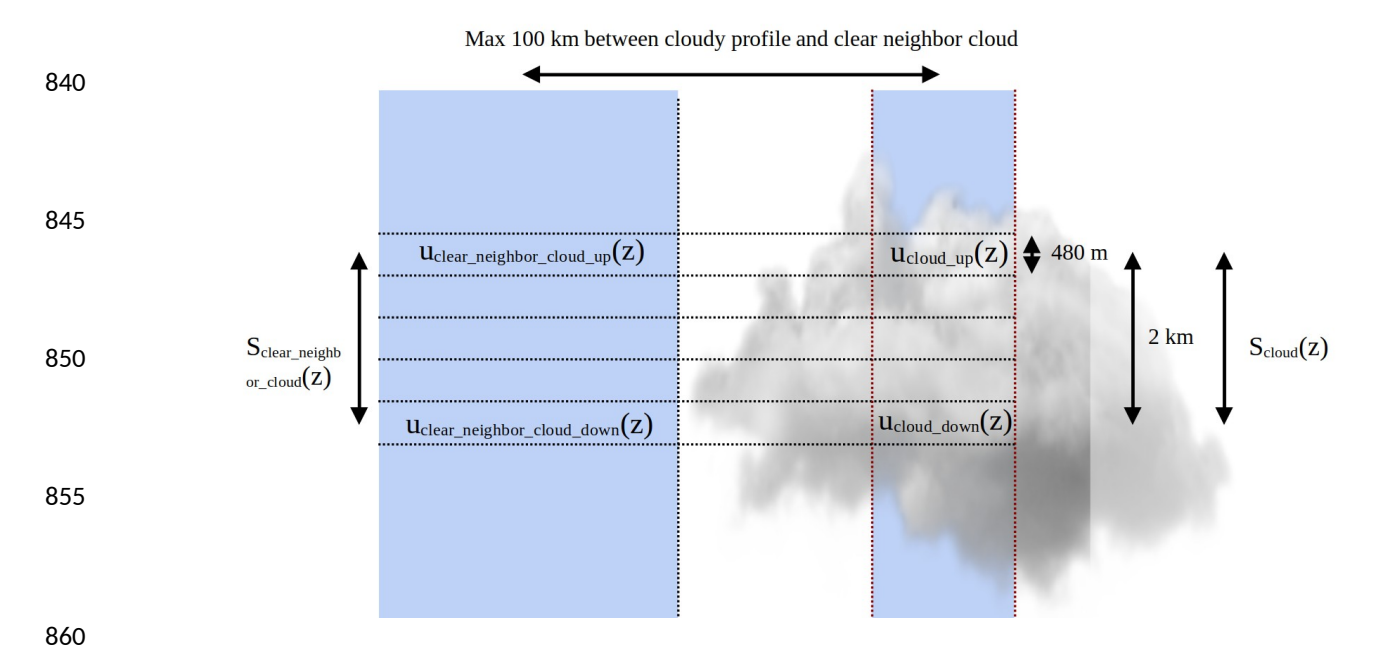


Figure B6: (a) complements relative to the calculations of wind shear within the cloud $S_{cloud}(z)$ and the surrounding clear sky wind shear $S_{clear_surrounding_cloud}(z)$





Data availability. ALADIN/Aeolus orbit files and gridded data presented in this paper are available via AERIS (https://dx.doi.org/10.25326/746). They are built from Aeolus Level 1A and Level 2B observations that can be accessed via the ESA Aeolus Online Dissemination System (https://aeolus-ds.eo.esa.int/oads/access/). CALIPSO-GOCCP version 3.1.4 (Chepfer et al., 2010) and ERA5 reanalyses (Hersbach et al., 2020) were accessible via Mesocentre ESPRI/IPSL.

Author contributions. ZT, MB and HC drafted the article. The Aeolus dataset development was performed by ZT and AGF. The data analysis was performed by ZT, MB, and HC. The WRF simulation was performed by SB and the airborne lidar data were collected by BW. All authors were involved in the writing and investigation.

885 *Competing interests.* The authors declare that they have no conflict of interest.

Acknowledgments. The authors thank Mesocentre ESPRI/IPSL for the computation resources. We also thank ESA dissemination team for the access to Aeolus data and AERIS for the storage of the dataset. We thank Dr. Louise Nuijens for the interesting discussions regarding convective momentum transport that participated to the motivations of this study. The authors thank the people involved in the production of the WRF simulation, performed on the HPC resources of TGCC under the allocations A0050106877 and A0070106877 made by GENCI. The authors also thank the DLR for the deployment of the Falcon and 2µm Doppler Wind Lidar during AVATAR-T campaign.

Financial support. This research was supported by European Space Agency and European Aeronautic Defence and Space company (EADS) in the framework of ZT's PhD.

895

890

880

900





910 References

- Abramian, S., Muller, C. and Risi, C.: Shear-Convection Interactions and Orientation of Tropical Squall Lines, Geophysical Research Letters, 49, https://doi.org/10.1029/2021GL095184, 2022.
- Aeolus Data Innovation and Science Cluster (Aeolus DISC): The Earth Explorer Mission Aeolus for atmospheric wind 915 observations Final Report from the Aeolus Data Innovation and Science Cluster DISC of Phase E, https://doi.org/10.57676/93c3-n766, 2024.
- Ali, S., Mehta, S. K., Ananthavel, A., and Reddy, T. V. R.: Temporal and vertical distributions of the occurrence of cirrus clouds over a coastal station in the Indian monsoon region, Atmos. Chem. Phys., 22, 8321–8342, https://doi.org/10.5194/acp-22-8321-2022, 2022.
 - Baars, H., Herzog, A., Heese, B., Ohneiser, K., Hanbuch, K., Hofer, J., Yin, Z., Engelmann, R., and Wandinger, U.: Validation of Aeolus wind products above the Atlantic Ocean, Atmos. Meas. Tech., 13, 6007–6024, https://doi.org/10.5194/amt13-6007-2020, 2020.
- Belova, E., Kirkwood, S., Voelger, P., Chatterjee, S., Satheesan, K., Hagelin, S., Lindskog, M., Körnich, H.: Validation of Aeolus winds using ground-based radars in Antarctica and in northern Sweden, Atmospheric Measurement Techniques, 14, 5415–5428, https://doi.org/10.1007/978-3-031-53618-2 6, 2021.
- Ban, N., Caillaud, C., Coppola, E., Pichelli, E., Sobolowski, S., Adinolfi, M., Ahrens, B., Alias, A., Anders, I., Bastin, S. et al.: The first multi-model ensemble of regional climate simulations at the kilometer-scale resolution, Part I: Evaluation of precipitation. *Clim. Dyn.* 57, 275-302, https://doi.org/10.1007/s00382-021-05708-w, 2021
 - Bony, S., Schulz, H., Vial, J., & Stevens, B.: Sugar, Gravel, Fish, and Flowers: Dependence of Mesoscale Patterns of Trade-Wind Clouds on Environmental Conditions, Geophysical Research Letters, 48, https://doi.org/10.1029/2019GL085988, 2020.
- Brueck, M., Nuijens, L. and Stevens, B.: On the Seasonal and Synoptic Time-Scale Variability of the North Atlantic Trade
 Wind Region and Its Low-Level Clouds, American Meteorological Society, 72, 1428-1446, https://doi.org/10.1175/JAS-D-14-0054.1, 2015.
 - Chepfer, H., Bony, S., Winker, D., Cesana, G., Dufresne, J. L., Minnis, P., Stubenrauch, C. J. and Zeng, S.: The GCM-Oriented CALIPSO Cloud Product (CALIPSO-GOCCP), Journal of Geophysical Research, 115, D00H16, https://doi.org/10.1029/2009JD012251, 2010.
- Chepfer, H., Cesana, G., Winker, D., Getzewich, B., Vaughan, M. and Liu, Z.: Comparison of Two Different Cloud Climatologies Derived from CALIOP-Attenuated Backscattered Measurements (Level 1): The CALIPSO-ST and the CALIPSO-GOCCP, American Meteorological Society, 30, 725–744, https://doi.org/10.1175/JTECH-D-12-00057.1, 2013.
- Chepfer, H., Brogniez, H. and Noel, V.: Diurnal variations of cloud and relative humidity profiles across the tropics, Nature Scientific Report, 9, https://doi.org/10.1038/s41598-019-52437-6, 2019.
 - Dabas, A., Ehlers, F., Flament, T., Trapon, D., Lacour, A., et al.: Optimization of Aeolus' aerosol optical properties by maximum-likelihood estimation. Atmos. Meas. Tech., 15, 185–203. https://doi.org/10.5194/amt-15-185-2022, 2022.



965



- Das, S.K., Chiang, C-W., and Nee, J-B.: Influence of tropical easterly jet on upper tropical cirrus: An observational study from CALIPSO, Aura-MLS, and NCEP/NCAR data, Journal of Geophysical Research, 116, https://doi.org/10.1029/2011JD015923, 2011.
- Donovan, D. P., van Zadelhoff, G.-J., and Wang, P.: The EarthCARE lidar cloud and aerosol profile processor (A-PRO): the A-AER, A-EBD, A-TC, and A-ICE products, Atmos. Meas. Tech., 17, 5301–5340, https://doi.org/10.5194/amt-17-5301-2024, 2024a.
- Donovan, D. P., van Zadelhoff, G.-J., and Wang, P.: Aeolus/ALADIN Algorithm Theoretical Basis Document Level 2A products AEL-FM, AEL-PRO, Document Version V2.00, https://earth.esa.int/documents/d/earth-online/aeolus-level-2a-algorithm-theoretical-baseline-document-ael-fm-and-ael-pro-products, 2024b.
 - Feofilov, A. G. and Stubenrauch, C. J.: Diurnal variation of high-level clouds from the synergy of AIRS and IASI space-borne infrared sounders, Atmos. Chem. Phys., 19, 13957–13972, https://doi.org/10.5194/acp-19-13957-2019, 2019.
 - Feofilov, A. G.: Interactive comment on "Characterization of dark current signal measurements of the ACCDs used on-board the Aeolus satellite" by Fabian Weiler et al., Atmos. Meas. Tech. Discuss., https://doi:10.5194/amt-2020-458-RC1, 2021.
- Feofilov, A. G., Chepfer, H., Noël, V., Guzman, R., Gindre, C., Ma, P.-L., and Chiriaco, M.: Comparison of scattering ratio profiles retrieved from ALADIN/Aeolus and CALIOP/CALIPSO observations and preliminary estimates of cloud fraction profiles, Atmos. Meas. Tech., 15, 1055–1074, https://doi.org/10.5194/amt15-1055-2022, 2022.
- Feofilov, A., Chepfer, H., Noël, V. and Hajiaghazadeh-Roodsari, M.: Towards Establishing a Long-Term Cloud Record from Space-Borne Lidar Observations, Space-based Lidar Remote Sensing Techniques and Emerging Technologies, 57–72, https://doi.org/10.1007/978-3-031-53618-2 6, 2024.
 - Flamant, P., Cuesta, J., Denneulin, M.-L., Dabas, A., and Huber, D.: ADM-Aeolus retrieval algorithms for aerosol and cloud products, Tellus A, 60, 273–288, https://doi.org/10.1111/j.1600-0870.2007.00287.x, 2008.
- Fujiwara, M., Xie, S.-P., Shiotani, M., Hashizume, H. and Hasebe, F.: Upper-tropospheric inversion and easterly jet in the tropics, Journal of Geophysical Research, 108, https://doi.org/10.1029/2003JD003928, 2003.
- Goldberg, R. A., Feofilov, A. G., Pesnell, W. D., and Kutepov, A. A.: Inter-hemispheric Coupling during Northern Polar Summer Periods of 2002–2010 using TIMED/SABER Measurements, J. Atmos. Sol.-Terr. Phys., 104, 277–284, https://doi.org/10.1016/j.jastp.2012.11.018, 2013.
 - Grubisic, V. and Moncrieff, M.W.: Parameterization of Convective Momentum Transport in Highly Baroclinic Conditions, Journal of the Atmospheric Sciences, 57, 3035–3049, <a href="https://doi.org/10.1175/1520-0469(2000)057<3035:POCMTI>2.0.CO;2">https://doi.org/10.1175/1520-0469(2000)057<3035:POCMTI>2.0.CO;2, 2000.
 - Guzman, R., Chepfer, H., Noel, V., Vaillant de Guélis, T., Kay, J. E., Raberanto, P., Cesana, G., Vaughan, M. A. and Winker D. M.: Direct atmosphere opacity observations from CALIPSO provide new constraints on cloud-radiation interactions, J. Geophys. Res. Atmos., 122, 1066–1085, https://doi.org/10.1002/2016JD025946, 2017
- Helfer, K. C., Nuijens, L., de Roode, S. R., and Siebesma, A. P.: How wind shear affects trade-wind cumulus convection. Journal of Advances in Modeling Earth Systems, 12, e2020MS002183. https://doi.org/10.1029/2020MS002183, 2020.



1025



- Hemanth Kumar, A., Venkat Ratnam, M., Sunilkumar, S.V., Parameswaran, K. and Krishna Murthy, B.V.: Role of deep convection on the tropical tropopause characteristics at sub-daily scales over the South India monsoon region,
- 1000 Atmos. Res., 14–24, https://doi.org/10.1016/j.atmosres.2015.03.012, 2015.
 - Hersbach, H., Bell, B., Berrisford, P., Hirahara, S., Horányi, A., Muñoz-Sabater, J., Nicolas, J., Peubey, C., Radu, R., Schepers, D., Simmons, A., Soci, C., Abdalla, S., Abellan, X., Balsamo, G., Bechtold, P., Biavati, G., Bidlot, J., Bonavita, M., Chiara, G., Dahlgren, P., Dee, D., Diamantakis, M., Dragani, R., Flemming, J., Forbes, R., Fuentes, M., Geer, A.,
- Haimberger, L., Healy, S., Hogan, R. J., Hólm, E., Janisková, M., Keeley, S., Laloyaux, P., Lopez, P., Lupu, C., Radnoti, G., Rosnay, P., Rozum, I., Vamborg, F., Villaume, S., and Thépaut, J. N.: The ERA5 global reanalysis. Q. J. Roy. Meteor. Soc., 146, 1999–2049, https://doi.org/10.1002/qj.3803, 2020.
- Hildebrand, P. H.: Shear-Parallel Moist Convection over the Tropical Ocean: A Case Study from 18 February 1993 TOGA COARE. Mon. Weather Rev., 126(7), 1952–1976. <a href="https://doi.org/10.1175/1520-0493(1998)126<1952:spmcot>2.0.co;2">https://doi.org/10.1175/1520-0493(1998)126<1952:spmcot>2.0.co;2, 1998.
 - Houze, R.A.: Mesoscale Convective Systems, Reviews of Geophysics, 42, https://doi.org/10.1029/2004RG000150, 2004
- Iwai, H., Aoki, M., Oshiro, M., and Ishii, S.: Validation of Aeolus Level 2B wind products using wind profilers, ground based Doppler wind lidars, and radiosondes in Japan, Atmos. Meas. Tech., 14, 7255–7275, https://doi.org/10.5194/amt-147255-2021, 2021.
- Koning, A. M., Nuijens, L., Mallaun, C., Witschas, B., & Lemmerz, C.: Momentum fluxes from airborne wind measurements in three cumulus cases over land. *Atmospheric Chemistry and Physics*, 22(11), 7373-7388. https://doi.org/10.5194/acp-22-7373-2022, 2022
 - Koren I., Oreopoulos, L., Feingold, G., Remer, L.A. and Altaratz, O.: How small is a small cloud?, Atmospheric Chemistry and Physics, 8, 3855–3864, https://doi.org/10.5194/acp-8-3855-2008, 2008.
 - Koren, I., Remer, L. A., Altaratz, O., Martins, J. V., & Davidi, A.: Aerosol-induced changes of convective cloud anvils produce strong climate warming. Atmospheric Chemistry and Physics, 10(10), 5001–5010. https://doi.org/10.5194/acp-10-5001-2010, 2010.
- 1030 Krisch, I., Hindley, N., Reitebuch, O. and Wright, C.: On the derivation of zonal and meridional wind components from Aeolus horizontal line-of-sight wind, Atmos. Meas. Tech., 15, 3465–3479, 2022 https://doi.org/10.5194/amt-15-3465-2022, 2022.
- Lux, O., Lemmerz, C., Weiler, F., Marksteiner, U., Witschas, B., Rahm, S., Geiß, A., and Reitebuch, O.: Intercomparison of wind observations from the European Space Agency's Aeolus satellite mission and the ALADIN Airborne Demonstrator, Atmos. Meas. Tech., 13, 2075–2097, https://doi.org/10.5194/amt-13-2075-2020, 2020.
 - McCoy, D. T., Eastman, R., Hartmann, D. L. and Wood, R.: The Change in Low Cloud Cover in a Warmed Climate Inferred from AIRS, MODIS, and ERA-Interim, Journal of Climate, 30, 3609-3620, https://doi.org/10.1175/JCLI-D-15-0734.1, 2017
- McGill, M. J., Yorks, J. E., Scott, V. S., Kupchock, A. W., and Selmer, P. A.: The Cloud-Aerosol Transport System (CATS): a technology demonstration on the International Space Station, Lidar Remote Sensing for Environmental Monitoring XV,



1055

1060

1065



edited by: Singh, U. N., International Society for Optics and Photonics, SPIE, 9612, 34–39, https://doi.org/10.1117/12.2190841, 2015.

- Mieslinger, T., Horváth, Á., Buehler, S. A., & Sakradzija, M.: The dependence of shallow cumulus macrophysical properties on large-scale meteorology as observed in ASTER imagery, Journal of Geophysical Research: Atmospheres, 124, 11477—11505. https://doi.org/10.1029/2019JD030768, 2019.
- 1050 Mitra, A. P.: Indian ocean experiment [INDOEX]: an overview, 2004, Indian J. Mar. Sci., 33, 30–39, 2004.
 - Noel, V., Chepfer, H., Chiriaco, M. and Yorks, J.: The diurnal cycle of cloud profiles over land and ocean between 51°S and 51°N, seen by the CATS spaceborne lidar from the International Space Station, Atmospheric Chemistry and Physics, 8, 9457–9473, https://doi.org/10.5194/acp-18-9457-2018, 2018.
 - Nuijens, L. and Stevens, B.: The Influence of Wind Speed on Shallow Marine Cumulus Convection, Journal of the Atmospheric Sciences, 69, 168–184, https://doi.org/10.1175/JAS-D-11-02.1, 2012.
 - Parker, D. J.: Cold pools in shear, Q. J. Roy. Meteor. Soc., 122, 1655–1674, https://doi.org/10.1002/qj.49712253509, 1996.
- Qu, X., A. Hall, S. Klein, and A. DeAngelis: Positive tropical marine low-cloud cover feedback inferred from cloud-controlling factors. *Geophys. Res. Lett.*, 42, 7767–7775, https://doi.org/10.1002/2015GL065627, 2015
 - Reitebuch, O.: The Spaceborne Wind Lidar Mission ADM-Aeolus, in: Atmospheric Physics. Research Topics in Aerospace, edited by: Schumann, U., Springer, Berlin, Heidelberg, https://doi.org/10.1007/978-3-642-30183-4 49, 2012.
- Ratynski, M., Khaykin, S., Hauchecorne, A., Wing, R., Cammas, J.-P., Hello, Y., and Keckhut, P.: Validation of Aeolus wind profiles using ground-based lidar and radiosonde observations at Réunion island and the Observatoire de Haute-Provence, Atmos. Meas. Tech., 16, 997–1016, https://doi.org/10.5194/amt-16-997-2023, 2023.
- 1070 Robe, F. R. and Emanuel, K. A.: The Effect of Vertical Wind Shear on Radiative-Convective Equilibrium States, Journal of the Atmospheric Sciences, 69, 1427–1445, https://doi.org/10.1175/1520-0469(2001)058<1427:TEOVWS>2.0.CO;2, 2001.
 - Rotunno, R., Klemp, J. B. and Weisman, M. L. A Theory for Strong, Long-Lived Squall Lines, Journal of the Atmospheric Sciences, 45, 463–485, <a href="https://doi.org/10.1175/1520-0469(1988)045<0463:ATFSLL>2.0.CO;2">https://doi.org/10.1175/1520-0469(1988)045<0463:ATFSLL>2.0.CO;2, 1988.
- Sathiyamoorthy, V., Pal, P. K. and Joshi, P. C.: Influence of the Upper-Tropospheric Wind Shear upon Cloud Radiative Forcing in the Asian Monsoon Region, 17, 2725–2735, <a href="https://doi.org/10.1175/1520-0442(2004)017<2725:IOTUWS>2.0.CO;2">https://doi.org/10.1175/1520-0442(2004)017<2725:IOTUWS>2.0.CO;2, 2004.
- Schulz, B., and Mellado, J. P.: Wind Shear Effects on Radiatively and Evaporatively Driven Stratocumulus Tops, Journal of the Atmospheric Sciences, 75, 3245–3263, https://doi.org/10.1175/JAS-D-18-0027.1, 2018.
 - Schumacher, R.S. and Rasmussen K.L.: The formation, character and changing nature of mesoscale convective systems, Nature Reviews Earth & Environment, 1, 300-314, https://doi.org/10.1038/s43017-020-0057-7, 2020
- Siebesma, P.A. et al.: A Large Eddy Simulation Intercomparison Study of Shallow Cumulus Convection, Journal of the Atmospheric Sciences, 60, 1201-12019, <a href="https://doi.org/10.1175/1520-0469(2003)60<1201:ALESIS>2.0.CO;2">https://doi.org/10.1175/1520-0469(2003)60<1201:ALESIS>2.0.CO;2, 2003



1105



- Stoffelen, A., Pailleux, J., Källen, E., Vaughan, M., Isaksen, L., Flamant, P., Wergen, W., Andersson, E., Schyberg, H., Culoma, A., Meynart, R., Endemann, M., and Ingmann, P.: The atmospheric dynamics mission for global wind field measurement, B. Am. Meteorol. Soc., 86, 73–88, https://doi.org/10.1175/BAMS-86-1-73, 2005.
 - Thorpe, A. J., Miller, M. J., Moncrieff, M. W.: Two-dimensional convection in non-constant shear: A model of mid-latitude squall lines, Q. J. Roy. Meteor. Soc., 108, 739–762, https://doi.org/10.1002/qj.49710845802, 1982.
- Voigt, A., Albern, N., Ceppi, P., Grise, K., Li, Y., Medeiros, B.: Clouds, radiation, and atmospheric circulation in the present-day climate and under climate change. WIREs Clim Change. 2021;12:e694. https://doi.org/10.1002/wcc.694, 2021.
- Wang, P., Donovan, D. P., van Zadelhoff, G.-J., de Kloe, J., Huber, D., and Reissig, K.: Evaluation of Aeolus feature mask and particle extinction coefficient profile products using CALIPSO data, Atmos. Meas. Tech., 17, 5935–5955, https://doi.org/10.5194/amt-17-5935-2024, 2024.
 - Wang, S., Golaz, J. C. and Wang, Q.: Effect of intense wind shear across the inversion on stratocumulus clouds, Geophysical Research Letters, 35, L15814, https://doi.org/10.1029/2008GL033865, 2008.
- Weiler, F., Kanitz, T., Wernham, D., Rennie, M., Huber, D., Schillinger, M., Saint-Pe, O., Bell, R., Parrinello, T and Reitebuch, O.: Characterization of dark current signal measurements of the ACCDs used on board the Aeolus satellite, Atmos. Meas. Tech., 14, 5153–5177, https://doi.org/10.5194/amt-14-5153-2021, 2021.
- Weisman, M. L. Rotunno, R., and Klemp, J. B.: "A Theory for Strong, Long-Lived Squall Lines" revisited, Journal of the Atmospheric Sciences, 55, 361–382, <a href="https://doi.org/10.1175/1520-0469(2004)061<0361:ATFSLS>2.0.CO;2">https://doi.org/10.1175/1520-0469(2004)061<0361:ATFSLS>2.0.CO;2, 2004.
 - Winker, D. M., Hunt, W. H., and Hostetler, C. A.: Status and Performance of the CALIOP Lidar, Proc. SPIE, 5575, 8–15, https://doi.org/10.1117/12.571955, 2004.
 - Witschas, B., Rahm, S., Dörnbrack, A., Wagner, J., and Rapp, M.: Airborne Wind Lidar Measurements of Vertical and Horizontal Winds for the Investigation of Orographically Induced Gravity Waves, J. Atmos. Ocean. Technol., 34, 1371–1386, https://doi.org/10.1175/jtech-d-17-0021.1, 2017.
- Witschas, B., Lemmerz, C., Geiß, A., Lux, O., Marksteiner, U., Rahm, S., Reitebuch, O., and Weiler, F.: First validation of Aeolus wind observations by airborne Doppler wind lidar measurements, Atmos. Meas. Tech., 13, 2381–2396, https://doi.org/10.5194/amt-13-2381-2020, 2020.
- Witschas, B., Lemmerz, C., Geiß, A., Lux, O., Marksteiner, U., Rahm, S., Reitebuch, O., Schäfler, A. and Weiler, F.: Validation of the Aeolus L2B wind product with airborne wind lidar measurements in the polar North Atlantic region and in the tropics, Atmos. Meas. Tech., 15, 7049–7070, https://doi.org/10.5194/amt-15-7049-2022, 2022.
 - Wood, R.: Stratocumulus clouds, Mon. Weather Rev., 140, 2373–2423, https://doi.org/10.1175/MWR-D-11-00121.1, 2012.